HIGH TEMPERATURE OXIDATION AND METAL DUSTING RESISTANCE OF TRADITIONAL IRON-BASED AND NOVEL ALUMINA FORMING AUSTENITIC ALLOYS

by

Wen-Chieh Lee

A Thesis Submitted in

Partial Fulfillment of the

Requirements for the Degree of

Master of Science

in Engineering

at

The University of Wisconsin-Milwaukee

August 2017

ABSTRACT

HIGH TEMPERATURE OXIDATION AND METAL DUSTING RESISTANCE OF TRADITIONAL IRON-BASED AND NOVEL ALUMINA FORMING AUSTENITIC ALLOYS

by

Wen-Chieh Lee

The University of Wisconsin-Milwaukee, 2017
Under the Supervision of Dr. Benjamin C. Church

Metal dusting is a catastrophic form of corrosion and carburization, and is a disintegration of alloys into a dust of metal particles, oxides and graphite deposition products. Metal dusting and related coking phenomenon happen in industrial fields where carburizing syngas appears in the process. Metal dusting would cause damage in the form of pits and notches in pipes and other metallic equipment often causing a loss of production time or reduced component lifetimes. It is of great importance to prevent this corrosion from happening to the metal materials used by the industry.

To counter the corrosion, a new generation of iron-based austenitic stainless steel alloys have been developed that are alumina formers. A series of alloys were selected to test the oxidation and metal dusting performance of these new alumina-forming-austenitic (AFA) materials and were compared to currently-available alloys often employed in these conditions. The nickel-iron-chromium austenitic stainless steels of 310 and 800H were purchased as wrought sheet samples and while the

chromia-forming HP alloy and alumina-forming G3607A and G3610A were centrifugally cast. Experimental high temperature oxidation and metal dusting atmospheres were set up using a tube furnace in order to observe the high temperature oxidation and metal dusting corrosion in these five different kinds of alloys. Oxidation test was conducted for 30 hours in a 950°C pure steam tube furnace environment. Industrial processes such as steam reforming, synthesis gas reaction, steam cracking used to generate clean fuels often use a similar kind of environment to form continuous oxide layers prior to exposing the materials to the high-carbon processes conditions. Metal dusting test was carried out under a H_2-CO-CO_2 environment at 650°C with carbon activity (a_c) of 10 for 500 hours. Mass changes from the oxidation and dusting tests were tracked.

Scanning Electron Microscopy (SEM), Energy Dispersive Spectroscopy (EDS), and X-ray Diffraction (XRD) were applied to characterize the oxide layers formed and the corrosion that occurred to the alloys. The alumina formers were able to form continuous protective oxide layer and also displayed less pits from metal dusting attack than the chromia formers. We can therefore conclude that when exposed to these metal dusting environment, the alumina-forming alloys could provide better corrosion resistance and is worth to be applied for economic and environmental advantages.

© Copyright by Wen-Chieh Lee, 2017
All Rights Reserved

To

My loving parents,

Shuyue Lee(S.Y. Lee) and Jinhui Liu(J.H. Liu)

whose words of encouragement and support

have inspired me to work hard for the things that I aspire to

achieve.

TABLE OF CONTENTS

LIST OF FIGURES ix

LIST OF TABLES xiv

LIST OF ABBREVIATIONS xv

ACKNOWLEDGMENTS xvi

CHAPTER 1. INTRODUCTION 1

1.1. Background 3

1.2. Oxidation mechanism 5

1.3. Metal dusting mechanism 7

1.4. Alloying additions 11

1.5. Chromium oxide vs alumina forming alloys 14

CHAPTER 2. EXPERIMENTAL PROCESS 15

2.1. Material composition 15

2.2. Sample preparation 17

2.3. Pre-testing measurements 19

2.4. Pre-oxidation test 22

2.5. Metal dusting test 25

2.6. Characterization

2.6.1. Change in mass 28

2.6.2. Optical Stereography 28

2.6.3. Scanning Electron Microscopy (SEM) 28
2.6.4. Energy Dispersive Spectroscopy (EDS) 28
2.6.5. X-Ray Diffraction(XRD)..... 29
CHAPTER 3. RESULTS 30
3.1. Change in mass 30
3.2. Optical stereoscope results 35
3.3. SEM results..... 39
3.4. EDS analysis..... 48
3.5. XRD analysis..... 58
CHAPTER 4. ANALYSIS AND DISCUSSION..... 61
CONCLUSIONS..... 66
FUTURE WORK..... 68
REFERENCES..... 69
APPENDIX A –FULL COMPOSITION OF FIVE ALLOYS..... 73
APPENDIX B –DIMENSIONS AND MASS OF SAMPLES..... 74

LIST OF FIGURES

Figure 1. Processed steps of metal dusting of pure iron and low alloyed steels with different cumulative exposure time 4

Figure 2. Illustration figure of Metal Dusting on alloy. (a)Example of metal dusting on the inner wall of a tube. (b) Pitting and metal wastage of an alloy 800 sheet caused by Metal Dusting 5

Figure 3. Model for illustrating diffusion-controlled oxidation 6

Figure 4. Processed steps of metal dusting of pure iron and low alloyed steels with different cumulative exposure time 9

Figure 5. The ternary diagram of operating metal dusting mechanisms of different composited alloys considered at the principal temperature 750°C 11

Figure 6. Isothermal section of Fe–Cr–C at 680°C. Dashed line shows a possible diffusion path for diffusion of carbon>> diffusion of metal 13

Figure 7: The comparison of growth rate and thermodynamic stability of Cr & Al oxide . 14

Figure 8. Notation for dimensions of samples after cutting 18

Figure 9. Appearance of the sample used for the tests 18

Figure 10. Specimen holder used to suspend the samples when react in the high temperature tube furnace 23

Figure 11. Oxidation apparatus..... 24

Figure 12. Illustration of the specimens put in the oxidation apparatus 25

Figure 13. Scheme of the metal dusting test furnace used 26

Figure 14. Metal dusting test apparatus..... 27

Figure 15. The overview of the testing sets run in this experiment 27

Figure 16. The mass change of alloys of oxidation test (Ox) 31
Figure 17.The mass change of alloys after oxidation continued with metal dusting test (Ox+MD) 32
Figure 18.The carbon deposition and removal of alloy HP after oxidation continued with metal dusting test (Ox+MD) 33
Figure 19.The mass change of alloys after only metal dusting test (MD) 34
Figure 20. Samples appearance in different stages- raw, post oxidation process, and post metal dusting 36
Figure 21. Optical stereoscope images of alloy 310 underwent oxidation and metal dusting tests, 500 μm scale 36
Figure 22. Optical stereoscope images of alloy 800H underwent oxidation and metal dusting tests, 500 μm scale 37
Figure 23. Optical stereoscope images of alloy HP underwent oxidation and metal dusting tests, 500 μm scale 37
Figure 24. Optical stereoscope images of alloy 2.6%Al underwent oxidation and metal dusting tests, 500 μm scale 38
Figure 25. Optical stereoscope images of alloy 3.9%Al underwent oxidation and metal dusting tests, 500 μm scale 38
Figure 26. SEM cross-section images of alloys after exposure to pure steam oxidation atmosphere at 950℃ for 30h 39
Figure 27. SEM top-view images of surface of alloys after exposure to pure steam oxidation atmosphere at 950℃ for 30h 40
Figure 28. SEM top-view images of surface of alloys after exposure to oxidation

continued with metal dusting test (Ox+MD), lower magnification (up) and higher magnification (down) images 42
Figure 29. SEM cross-section images of surface of alloys after exposure to oxidation continued with metal dusting test (Ox+MD), lower magnification (up) and higher magnification (down) images 43
Figure 30. SEM top-view images of surface of alloys after only metal dusting test (MD), lower magnification (up) and higher magnification (down) images 45
Figure 31. SEM cross-section view images of surface of alloys after only metal dusting test (MD), lower magnification (up) and higher magnification (down) images 46
Figure 32. SEM top-view images of surface of alloys, remove the carbon deposition after only metal dusting test (MD), lower magnification (up) and higher magnification (down) images 47
Figure 33. SEM cross-section image of alloy 310 post-oxidation with EDS analysis, (a) spot analysis, (b) and (c) are line scan analysis 48
Figure 34. SEM cross-section image of alloy 800H post-oxidation with EDS analysis, (a) spot analysis, (b) and (c) are line scan analysis 49
Figure 35. SEM cross-section image of alloy HP post-oxidation with EDS analysis, (a) spot analysis, (b) and (c) are line scan analysis 50
Figure 36. SEM cross-section image of alloy 2.6%AI post-oxidation with EDS analysis, (a) spot analysis, (b) and (c) are line scan analysis 51
Figure 37. SEM cross-section image of alloy 3.9%AI post-oxidation with EDS analysis, (a) spot analysis, (b) and (c) are line scan analysis 52
Figure 38. SEM top-view images of alloys post-oxidation with EDS spot and region analysis 53

Figure 39. SEM cross-section image of alloy 310 after Ox+MD test with EDS analysis, (a) spot analysis, (b) and (c) are line scan analysis of the oxide layer; while (d) and (e) are line scan of the pit..... 55
Figure 40. SEM cross-section image of alloy 800H after Ox+MD test with EDS line scan analysis..... 56
Figure 41. SEM cross-section image of AFA alloys after Ox+MD test with EDS line scan analysis..... 57
Figure 42. XRD diagrams obtained by analyzing alloys' surface after exposure to oxidation environment (Ox) 59
Figure 43. XRD diagrams obtained by analyzing alloys' surface after exposure to metal dusting environment (MD) 60
Figure 44. Positions mapping of the SEM images of post-oxidation samples, cross-section image(left); top-view image(right) 63
Figure 45. Comparison of samples went through pre-oxidation plus metal dusting, and went through only metal dusting, Oxidation+ Metal dusting(upper images); Only metal dusting(lower images) 65

LIST OF TABLES

Table 1. Chemical compositions of the selected alloys (wt%) 16

Table 2. Alloys with different nickel to iron ratio (%), chromium content (wt%), and aluminum content (wt%) 17

Table 3. Sample designations by giving notations 19

Table 4. Samples' dimensions and calculated surface area 21

Table 5. Mass of samples measured prior to the tests 22

Table 6. Oxide layer formation and average thickness results 62

Table 7. Internal oxidation formation and approximately reached depth results 63

Table 8. Theoretical equation applied to predict the resistivity to metal dusting 65

Table 9. Alloys' full composition 73

Table 10. Samples' dimensions, calculated surface area, and initial mass 74

LIST OF ABBREVIATIONS

SS	Stainless Steel
HP	High Performance Heat-resistant chromia-forming alloys
AFA	Alumina-forming austenitic stainless steel alloy

ACKNOWLEDGMENTS

I would first like to thank to my advisor Dr. Benjamin Church for accepting me into his research group. His continuous advices and caring help support me to face and pass the obstacles arose from the change of my study field and study environment. Being generously taught about academic knowledge and experimental procedure, I can finally finish my thesis and defense, and become a better person in this place. I can't help to think of and agree on a comment that I used to have heard on Dr. Church: "He is a teacher that really care about his student and give support.".

I would like to thank my committee members Dr. Nidal Abu-Zahra and Dr. David Yu. Thanks to Dr. Abu-Zahra for considering and approving my admission to study in this department in the first beginning and give good suggestion upon my research results and the direction toward future work. Thanks to Dr. Yu for his support during my Master's studies.

I would also like to thank Jim Myers of MetalTek for providing his industrial knowledge and resources for the project and experiment. I also want to thank Dr. Steven Hardcastle for supporting with his knowledge and time on the SEM, EDS and XRD operating procedures in the AAF.

I would like to thank the research group members, Kao Yang, Lizeth Ortiz, and Elmer Prenzlow, for their continuous help on solving my questions and difficulty as a foreign student and the friendship they enthusiastically offer. Every result shown in this thesis was achieved with their support.

I also want to express the appreciation for the persons who care about me most, my families in far Taiwan and my girlfriend Le Gong as a senior student at UWM, I will never finish the research project without their emotional and material assistance.

CHAPTER 1. INTRODUCTION

Industrial-related applications such as power generation, oil refining, carbon capture and storage, chemical processing and fuel cell applications contain the usage of metal materials. In which these metals are introduced to high temperature reactions and exposed to the gaseous environment that cause corrosion and restrict the material's functionality and reduce the efficiency of the system. Metal dusting is a catastrophic form of corrosion and carburization, and is a disintegration of alloys into a dust of metal particles, oxides and graphite deposition in a carbonaceous atmospheres. The metal dusting and related coking phenomenon happen in the industrial fields where carburizing syngas appear in the reacting processes (1). Metal dusting would cause damage in the form of pits and notches in pipes and other metallic equipment and therefore losing production time. It is of great importance to prevent this corrosion to the metal materials used by the industry. Typical materials used in these industrial application as pipes and tubes would be austenitic Fe-Ni-Cr alloys. When exposed to synthetic gas environment with a specific temperature ranged 400°C to 800°C and have a sufficiently high carbon activity(a_c), metal dusting of these alloys could occur. Detail studies about metal dusting were conducted by modern researchers such as Grabke et. al (2). These coordinated gaseous environment will lead to the formation of metastable M_3C-type carbides upon alloy's surface as a result of the disintegration of the base alloy. After the carbides form, with the variation and lowering in carbon activity to the level of $a_c=1$, the unstable carbides will decompose and form graphite. With longer time periods, the corrosion will come to a stable state and filamentous product such as carbon nanotubes will form (3). To reduce metal dusting corrosion to the alloy, there are some different preventing ways could be applied and have been investigated. One of the methods is adding elements into the alloy as additions to change the alloy's resistance to the metal

dusting. For instance, researchers Zhang et. al (4) and Nishiyama et al. (5) have respectively shown that the copper addition of nearly 10% to 20% to the nickel based alloy could effectively reduce the coking deposition and metal dusting phenomenon. Another way to reduce metal dusting is the formation of protective oxide layers. With an effective oxide layer formed on the surface of the base alloy, carbon produced from carburizing atmosphere is less able to penetrate to the metal surface to form M_3C which is the catalyst for later graphitization and dusting phenomenon. Protective oxide scales such as Cr_2O_3 or SiO_2, could be formed from the reaction of chromium or silicon, respectively, in the oxidizing environment and in the process of carburization. Aluminum could also form Al_2O_3 which could have increased stability in the higher temperature range and more resistant to water vapor oxidation (6), and therefore not only chromia-forming alloys but also alumina-forming alloys have been widely discussed by researchers. Schillmoller et al. (7) have proposed an modified equivalent equation of the alloy's content : $Cr\% + 3 \times (Si\% + Al\%) > 24$, as a referenced criterion to see if it satisfy and can resist to the metal dusting well. The improvement of the performance of traditional iron and nickel based alloys and current chromia and alumina forming alloys are valuable for commercial perspectives and their resistance to high temperature corrosion is definitely worth for observation.

1.1. Background

Metal dusting is a kind of corrosion phenomenon resulting from carbonaceous reaction, and being more specific, synthesis gas reaction. With environmental issues such as global warming continuing to grow, it is of importance for foundries and industrial companies to apply related refinery processes that can transfer polluting feedstocks such as natural gas into clean fuels such as diesel fuels or methanol. Take Gas To Liquids (GTL) process as an example, it is a process that contains steam reforming and synthesis gas reaction. As illustrated in Figure 1 (8), natural gas such as methane (CH_4) will be reformed at the temperature of 1000°C or higher and partially oxidized to carbon dioxide, hydrogen and carbon monoxide gases and water, which constitute the synthesis gas environment. Then synthesis reaction will occur. When the temperature of the reaction goes down to the range of 800°C to 400°C, a form of corrosion called metal dusting (MD) can appear. The Energy Economics and Forecasting Department (EEFD) have made a measurement and reported that in the next 25 years, from 2016 to 2040, the annual global demand for gas will increase to the level about 5,200 billion cubic meters (bcm). With the increase of more than 50% compared to 3,500 bcm in 2015. (9) It makes it much more important to know how to deal with such synthesis gas side reactions as metal dusting, when people have more demand on producing usable clean fuels by transferring from natural gas resources.

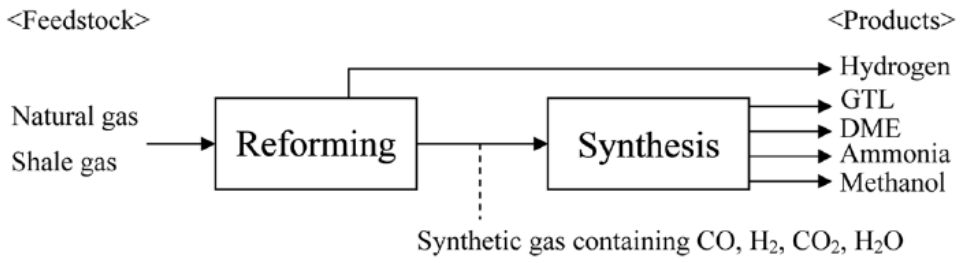

Figure 1. Processed steps of metal dusting of pure iron and low alloyed steels with different cumulative exposure time (8)

The phenomenon of metal dusting could be very dangerous and can lead to perforation of tubes or walls in a few days (Figure 2). Metal dusting has been observed in different kinds of plants which are involved in energy production and heat-treating equipment. A general definition of the Metal Dusting and the factors involved were presented at the annual NACE conference in 1963 (10), which can be summarized as (3):

1. Temperature: Typically 450°-800°C
2. Environment: In the gaseous state, potentially reducing and carburizing with or in the absence of oxygen
3. Product: Powder or dust composed of metal oxides, metal carbides as well as a mixture of graphite and metal
4. Form: General pitting, localized or total surface damage or carburization

(a) (b)

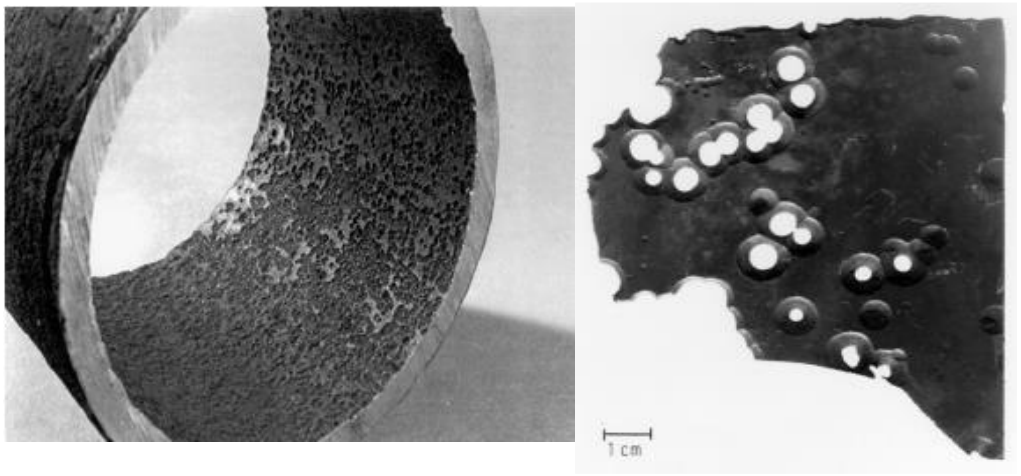

Figure 2. Illustration figure of Metal Dusting on alloy. (a)Example of metal dusting on the inner wall of a tube. (b) Pitting and metal wastage of an alloy 800 sheet caused by Metal Dusting. (2)

1.2. Oxidation Mechanism

The most common oxidation law we apply would be the Wagner oxidation model which assumes that the rate at which the oxide layer could formed is controlled by the diffusion of metallic ions and oxygen ions through the oxide layer (11). The equation (1.1) denote the basic kinetics of the Wagner oxidation model, in which it can be applied to estimate the relationship between oxide layer thickness (Δx) and the oxidation time (Δt).

$$\Delta x = k_p \Delta t^{1/2} \qquad (1.1)$$

Also, the Wagner oxidation theory has interpreted that the rate determining step in an

oxidation process is controlled by diffusion of ions through an oxide layer as shown in Figure 3.

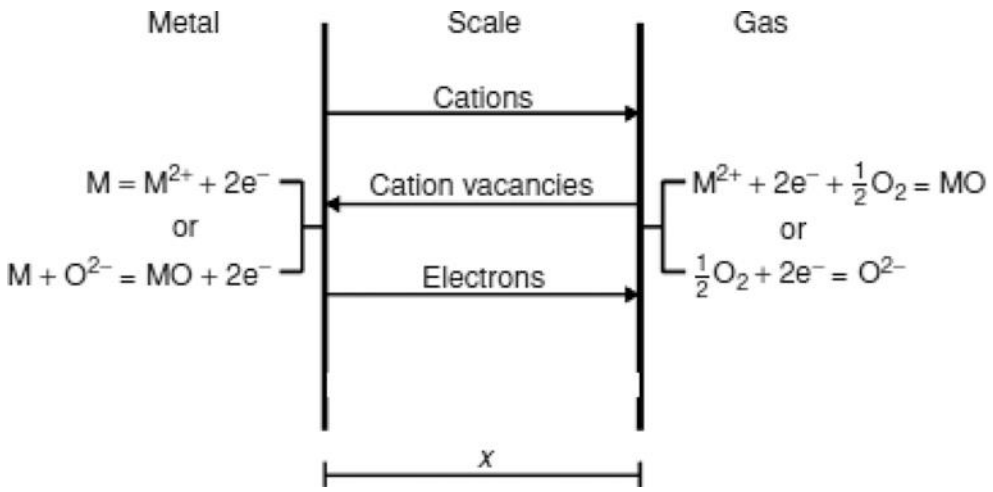

Figure 3. Model for illustrating diffusion-controlled oxidation (12)

The oxidation phenomenon is a common but an important issue when dealing with corrosion of alloys. This corrosion form usually occur at high temperature and could be decisive for determining the durability of heat resistant alloys. The metals and alloys will tend to be oxidized when exposed to air or environments with high oxygen potential and considerable temperature degree which serve as a key factor on determining what kind of oxidize layer will be grown on the surface of metal (13). Observations could be done on a post-oxidized sample to see if a continuous external layer of stable oxidized product was formed to determine alloy's oxidation resistance (14). For high-temperature applications, such as air and steam environment that has temperature higher than 600 °C, Cr_2O_3 and Al_2O_3 are the principal oxides used for the protection of metallic alloys (14).

1.3. Metal dusting mechanism

This corrosion form can be essentially described as a break-up of bulk metal to metal powder. Deposition of a graphite layer on the surface of the metal, usually from carbon monoxide (CO) in the vapor phase is the first aspect of the mechanism. According to the early research by R.F. Hochman et al. (15), this graphite layer was considered to form metastable M_3C species (where M is the metal such as Fe), which migrate away from the metal surface. However, in some regimes such as nickel alloys, there might be no M_3C species observed and thus indicating a direct transfer of metal atoms into the graphite layer. This catastrophic carburization causes pitting or uniform thinning of iron-based or nickel-based alloys. The corrosion products could be carbonaceous deposits (coke) containing very fine metallic particles. More specifically, the phenomenon of metal dusting may be divided into three main mechanisms denoted Type I, Type II and Type III. Type I, can be noted as decomposition of metastable carbides, first described by Hochman (15) and further refined by Grabke (2). This mechanism can be summarized as first forming the metastable cementite and then the decomposition of the previously formed metastable cementite into graphite and iron during metal dusting conditions. Type II, can be noted as graphite formation into and inside thermodynamically stable phases, describing the disintegration of a carbon supersaturated phase by precipitated graphite. Neither carbides nor oxides are thermodynamically stable in Ni alloys or Fe–Ni austenite alloys under metal dusting conditions, only metal and graphite are stable. This Type II degradation mechanism may be described as graphite formation into and inside the carbon-saturated metal matrix, which leads to very small metal fragments surrounded by graphite. This mechanism was described by Hillert et al. (16) in the 1950's and studied in detail by Pippel et al. (17). Type III operates on high alloyed steels and Ni-base alloys and involves selective oxidation of alloyed carbides. This mechanism is based on the concept of active corrosion under the

influence of both carbon and oxygen. Carbon reacts with metal and metal carbides are formed. These carbides dissolve and oxidize selectively and free carbon is released which forms carbides/graphite and so forth. The possible active role of oxygen during metal dusting is the fundamental concept of the Type III metal dusting mechanism. It should be mentioned that there is seldom only one MD mechanism operating on a steel. For example, Types II and III operate conjointly in austenitic stainless steels and Ni-base alloys (18). As shown and explained by Szakálos(3), for pure iron and low alloyed steels, there could be several steps occurring in order when exposure to metal dusting environment as shown in Figure 4. At time = t1, cementite starts to form at the surface when the activity of carbon exceeds 1.7. Further along the temperature profile at t2, the cementite layer approaches to maximum thickness and starts to form graphite. At t3 the graphite grows to a certain thickness the carbon activity drops to a unity and decomposition of the cementite occurs (an example of Type I mechanism). This decomposition is a eutectoid reaction at t4 and forms an intermediate eutectoid layer where cementite breaks down into ferrite and graphite. At t5, the cementite is depleted and left with just the ferrite and coke. Finally, at t6 the corrosion and corrosion products come to a steady state size and porosity which is the result of the metal dusting process. In the other hand, for pure nickel or nickel-based alloy, there could be several properties that lead to directly decomposition of the base material by graphitization, but not underwent an instable carbides formation (19). Properties such as no formation of carbides and no formation of effective protective oxides will promote the Type II mechanism, disintegration of a carbon-supersaturated matrix by internal graphite formation (3).

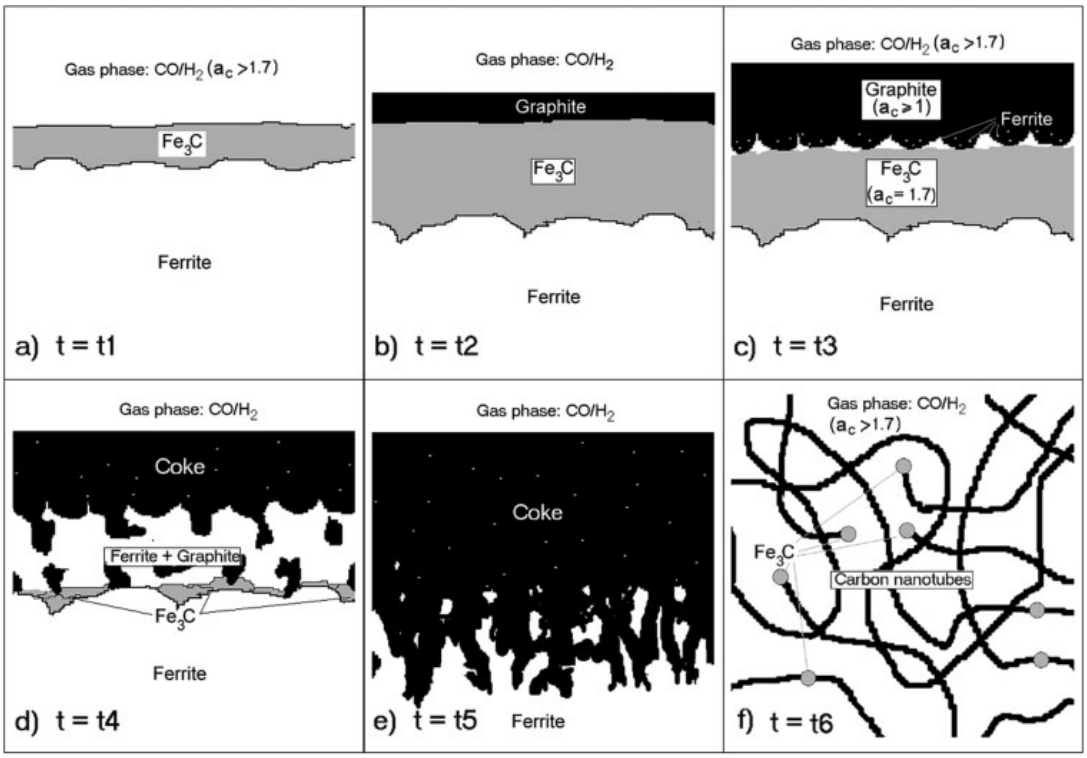

Figure 4. Processed steps of metal dusting of pure iron and low alloyed steels with different cumulative exposure time (3)

To define the mechanism for the occurring of metal dusting corrosion, we have to consider what kind of environment that testing alloys will be exposed to. We usually need to consider not only the temperature but also the gas mixture, the carbon activity (a_c) and the oxygen partial pressure (P_{O2}). In the related carbonaceous reaction like metal dusting, the carbon activity could be calculated using two main reaction equation which contribute the carbon deposition are 1) the synthesis gas reaction, in which the reduction of CO by hydrogen was demonstrated and 2) the Boudouard reaction, in which carbon monoxide reacts to form carbon dioxide and carbon. These two reaction equations are listed below:

(1) The synthesis gas reaction:

$$H_2 + CO = H_2O + C \qquad (1.2)$$

and therefore carbon activity(a_c), could be calculated as :

$$a_c = \frac{K \times P_{co} \times P_{H2}}{P_{H2O}}$$

where K is the equilibrium constant and P_i is the partial pressure of the specific gas.

(2) The Boudouard reaction :

$$2CO = CO_2 + C \qquad (1.3)$$

and thus the carbon activity(ac), could be calculated as :

$$a_c = \frac{K \times P_{co}^2}{P_{CO2}}$$

Following the investigation of Szakálos et al. (20) on the kinetics of these reactions as a function of CO/H_2 content and temperature of pure iron. The results showed that synthesis gas reaction dominates at higher H_2 concentrations while the Boudouard reaction dominates at higher CO concentrations (20). In determining the oxygen partial pressure (P_{O2}), there are also two main situations that need to be considered and classified. In the $CO–H_2–CO_2–H_2O$ gas mixture, the oxygen partial pressure can be calculated using equation (1.4) with the presence of H_2O. While exposed to a gas mixture like $CO–H_2–CO_2$, the oxygen partial pressure can be calculated using equation (1.5) in the absence of H_2O. (21)

$$H_2O = H_2 + 1/2O_2 \qquad (1.4)$$

and thus $P_{O2} = (\frac{K \times P_{H2O}}{P_{H2}})^2$

$$CO_2 = CO + 1/2O_2 \qquad (1.5)$$

and thus $P_{O2} = (\frac{K \times P_{CO2}}{P_{CO}})^2$

The alloy composition and exposure temperature could determine which type of metal dusting mechanism is dominant. (3) It has been reported that metastable cementite could not be formed above the temperature of 750℃ (22) Therefore, this temperature could be seen as a principal change point for the occurring of type I mechanism as shown in Figure 5. The higher iron concentration alloys will first undergo the relatively faster reaction of type I mechanism, while for the alloys which contain higher nickel or higher chromium, it will move to the slower reaction of type II and type III mechanism at the temperature ranged below 750℃. For instance, alloy 800H will not only undergo mechanism I due to its multiple element composition, but might experience mechanism III in different time periods.

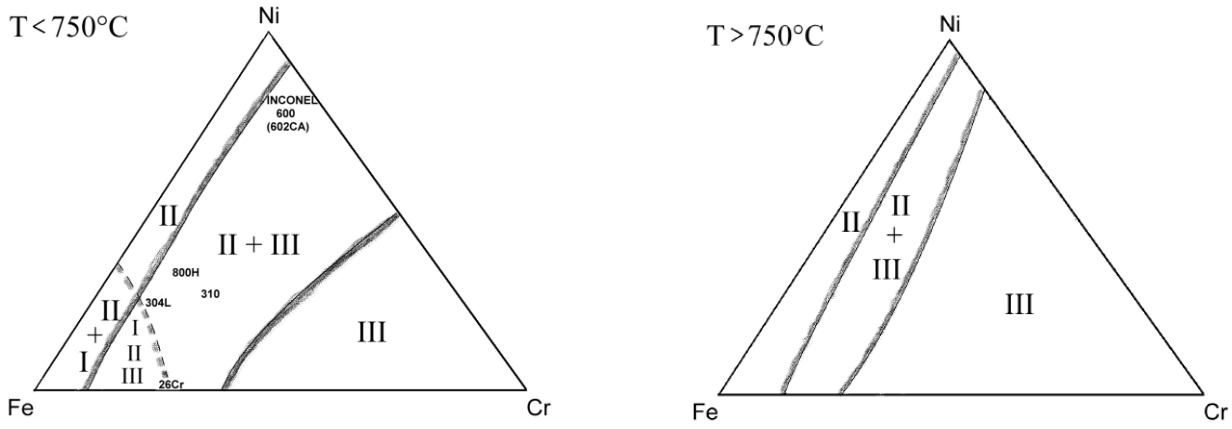

Figure 5. The ternary diagram of operating metal dusting mechanisms of different composited alloys considered at the principal temperature 750°C (3)

1.4. Alloying additions

Toh et. al (23) studied Fe-Cr and Fe-Ni-Cr alloys under 68%CO-26%H_2-6%H_2O gas mixtures at 680 °C (a_c = 2.9) under thermal cycling conditions. Depending on the composition of the alloy and the Fe/Cr ratio, a diffusion path may be decided in the ternary

diagram of the Fe-Cr-C system. According to Figure 6 listed below, the corresponding diffusion path for an Fe-46Cr alloy is shown. The reason why the point of 46% chromium content is critical is because at points lower than this chromium level, the formation of Fe_3C will occur while it will not form at higher levels. Therefore, iron-based alloys containing more than 46% Cr would be predicted to resist dusting. However, with additions of nickel to the Fe-Cr-C system would results in destabilization of both ferrite and Fe_3C. With nickel composition amount from 10 and 25%, the Fe_3C phase is completely suppressed and only the chromium-rich carbides are predicted to form under the conditions of the test. They concluded that loss of chromia-reheating ability was followed by spinel formation, internal carburization, and surface cementite formation was found on the alloys after being tested.

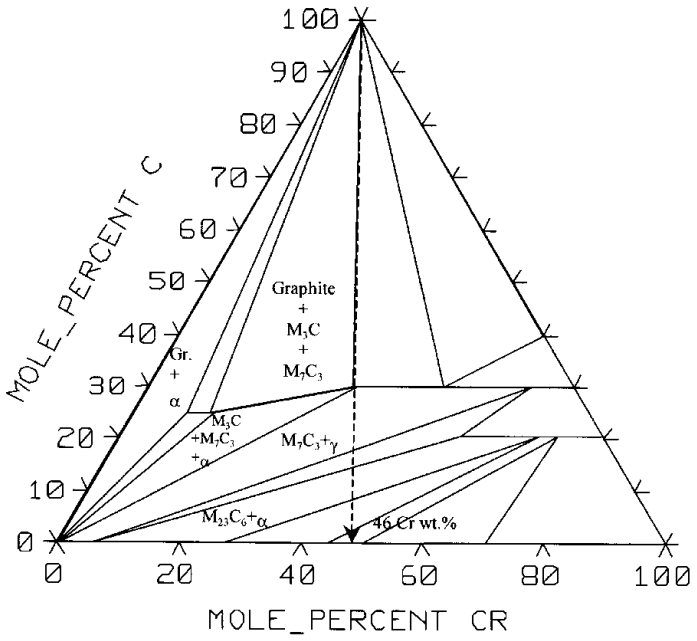

Figure 6. Isothermal section of Fe–Cr–C at 680°C. Dashed line shows a possible diffusion path for diffusion of carbon>> diffusion of metal

Mulaudzi et al (24) studied an clear observation on the initial stage of metal dusting of alloys 602CA and 800H. The carbonaceous environment is consisted with the gas mixture of 18.9%CO, 79.1%H_2, and 2% H_2O at 650°C with carbon activity, a_C = 11.75. The results show that aluminum-content alloy 602CA was found to be able to form alumina, chromia, and titanium oxide as protective oxide layer and being more resistant to metal dusting, while chromium-content alloy 800 has detected to form FeNi, Fe_2O_3, F_3O_4, and graphite and start to be attacked even in a relatively short period of time of 96 hours. The detection of formation of these spinel structures also reveal that the formation of spinel is negative to the formation of Cr_2O_3, and therefore suffer from metal dusting.

1.5. Chromium oxide vs alumina forming alloys

Chromium oxide, in the form of chromia (Cr_2O_3), is commonly used as a protective oxide layer and was formed on the surface of the pipes and tubes to resist the oxidized, carbonaceous, kinds of corrosion in high temperature environment. The process of chromium oxide forming is generally applied when petrochemical pipes are being cast and built. Although the chromia layer provide descent protective ability at relatively high temperature, it still have some weakness that can be improved. Chromium oxide sometimes could be formed with the presence of side product, such as carbides and spinel compound. The presence of byproducts will thus decrease it's stability. Furthermore, there might be degradation happen to chromium oxide and increase the attack of internal oxidation (25). Different from chromia, aluminum oxide could be formed with less amount of aggressive species as byproduct and therefore could be more resistant to corrosions. In the meanwhile, alumina is more thermodynamically stable in oxygen at elevated temperatures. Although alumina scale grows at a much slower rate than chromia, usually one to two orders of magnitude slower, as Figure 7 illustrate. (26) Aluminum oxide is also more resistant to water vapor. Alumina-forming alloys drag attention out of these benefits.

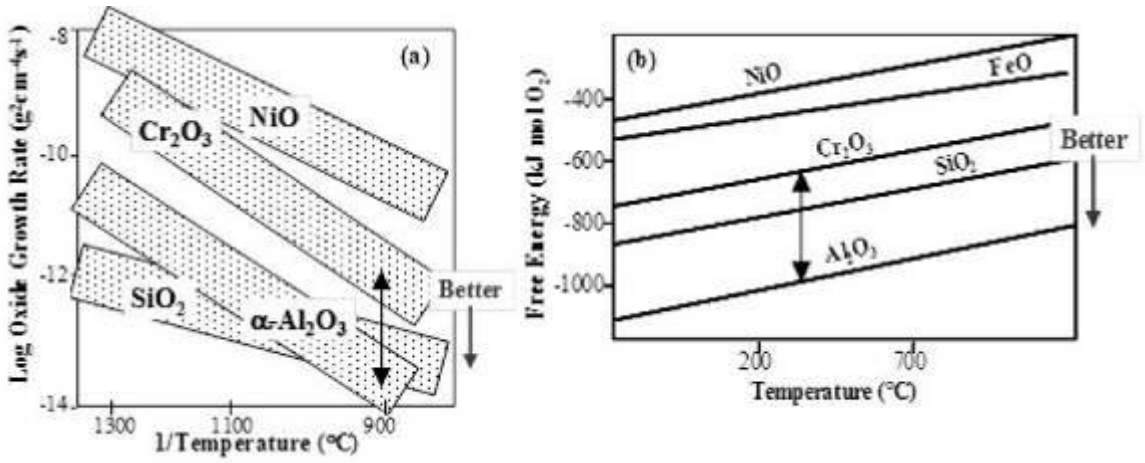

Figure 7. The comparison of growth rate and thermodynamic stability of Cr & Al oxide (26)

CHAPTER 2. EXPERIMENTAL PROCESS

Experimental high temperature oxidation and metal dusting atmospheres were set up using a tube furnace in order to observe the high temperature oxidation and metal dusting corrosion in five different kind of alloys, which included austenitic heat-resisting stainless steel, nickel-iron-chromium, chromia-forming, and alumina-forming alloys. Comparing different metallic behavior results arose from exposing these five alloys with different chemical composition to oxidation, metal dusting, and oxidation collaborate with metal dusting environments. Oxidation test was conducted in a 950°C pure steam tube furnace environment, in which the development of continuous oxide layer has been shown before (27). Metal dusting test was carried out under a H_2-CO-CO_2 environment at 650°C with carbon activity(a_c) equal to 10. Previous researches on the metal dusting resistance of nickel-iron-chromium (23) and alumina-forming alloys (28) as references providing possible environment settings for observing the metal dusting corrosion. After the exposure, the specimens were characterized using SEM and EDS to examine the formation of oxide layer, metal dusting attack in the form of pits and notches, and changes to the base materials. XRD was also conducted to analyze the internal composited structure of the layers.

2.1 Material Composition

A series of alloys were selected to test the oxidation and metal dusting kinetics. The nickel-iron-chromium austenitic stainless steels of 310 and 800H were purchased as rolled sheet; while the chromia-forming HP alloy and alumina-forming G3607A and G3610A were produced through centrifugal casting process and provided by MetalTek International, were received as sections of pipe. These five different alloys were intentionally designed as materials for constructing pipes and tubes for industrial

purposes. The alloys' chemical compositions are shown in Table 1.

Table 1. Chemical compositions of the selected alloys (wt%)

Element / Alloy	Al	C	Cr	Fe	Mn	Mo	Ni	Si	Other
310	0	0.05	24.52	51.0	1.8	0.01	19.10	0.6	
800H	0.54	0.07	20.63	46.6	0.6	0	30.33	0.3	
HP	0.02	0.44	26.52	35.08	0.6	0.11	34.50	1.3	Nb:0.8
2.6%Al	2.62	0.43	28.00	26.85	0.8	0.17	38.26	1.3	Nb:0.8
3.9%Al	3.9	0.44	27.40	24.93	0.8	0.19	38.01	1.4	Nb:0.8

As shown in Table 2, 2.6%Al and 3.9%Al represent the G3607A and G3610A which are designed as alumina-forming austenitic alloys (AFA) containing 2.6% and 3.9% of aluminum. HP is a chromia-forming alloy. 310 and 800H are nickel-iron-chromium austenitic stainless steels. These five different alloys were chosen as they contain lowest to highest aluminum content, chromium content, and Ni-Fe ratio as shown in Table 2. By comparing the resistance test results of 310 and 800H, we can find out how the difference in the amount of Cr content and Ni content will affect the formation of oxide layer and the resistance to metal dusting. Previous researches have shown that the different content of Ni and Cr of the alloys might result in different level of metal dusting corrosion (23),(29). In addition, by making a cross-comparison of resistance test between chromia-forming HP alloy which contain higher amount of Cr and Ni and alumina-forming alloys which contain great amount of aluminum, we can further conclude the formation and functionality of more protective of chromia and alumina. Mass change of the specimens were recorded during all steps of the experiments.

Table 2. Alloys with different nickel to iron ratio (%), chromium content (wt%), and aluminum content (wt%).

Alloy	Ni-Fe Ratio	Cr content	Al content
310	0.3745	24.52	0
800H	0.6509	20.63	0.54
HP	0.9835	26.52	0.02
2.6%Al	1.4250	28.00	2.62
3.9%Al	1.5250	27.40	3.9

2.2 Sample preparation

Alloys were cut from as-cast pipe sections into small specimens using a diamond cutting saw for later experiment with the dimension of near 7 mm in width, near 14 mm in length and near 1.5 mm in thickness. There is a round hole in the surface of each specimen drilled by a bench drilling machine with a diameter of 1mm for the later hanging purpose (sample's appearance shown in Figure 9). Variables "*w*' and "*l*" represent the width and length; "*t*" the thickness of the samples and "*h*" the diameter of the inner hole. Following this, samples were ground to 600-grit in all sides of the cut surfaces, and cleaned with hand soap followed by methanol and by acetone. For one kind of alloy in one specific testing environment, there are two in amount of the samples prepared for the test. By preparing two samples, we can average the mass change and get the uniform results of the property change for one testing condition.

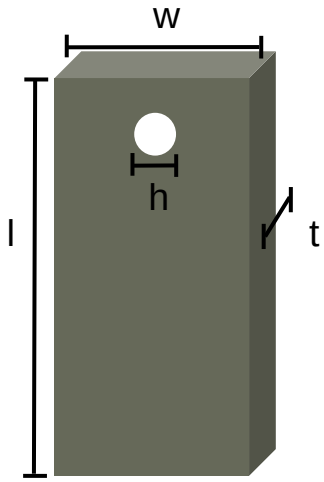

Figure 8. Notation for dimensions of samples after cutting

Figure 9. Appearance of the sample used for the tests

In order to track samples throughout each testing set of oxidation, oxidation continued with metal dusting, and metal dusting. Each sample was given a part number as a notation which included the alloy's name, testing set, time and temperature. Additionally, each sample was assigned a notation combined with one letter and one number from A1 to E6, samples with mark "A" represent the alloy 310, mark "B" represent the alloy 800H, mark "C" represent

the alloy HP, mark “D” represent the alloy G3607A(2.6%Al), and mark “E” represent the alloy G3610A(3.9%Al), as listed in Table 3.

Table 3. Sample designations by giving notations

Sample	Alloy	Testing set	Time (h)	Temperature (°C)
A1	310	Oxidation	30	950
A2				
B1	800H			
B2				
C1	HP			
C2				
D1	2.6%Al			
D2				
E1	3.9%Al			
E2				
A3	310	Oxidation , continued with Metal dusting	30 for oxidation and 500 for metal dusting	950 for oxidation and 650 for metal dusting
A4				
B3	800H			
B4				
C3	HP			
C4				
D3	2.6%Al			
D4				
E3	3.9%Al			
E4				
A5	310	Metal dusting	500	650
A6				
B5	800H			
B6				
C5	HP			
C6				
D5	2.6%Al			
D6				
E5	3.9%Al			
E6				

2.3 Pre-testing measurements

Prior to the oxidation and metal dusting test, samples were subjected to the measurements of surface area and initial mass. Each sample was assumed to have a rectangular shape

with a round drilled hole in the upper middle area as shown in Figure 8. After being drilled a hole through the body, samples were ground until all sides were flat in the ease for the later exposure experiment. Surface area of each sample was calculated using equation (2.1).

$$SA = 2 * [(w * l - h * \pi) + (w * t) + (l * t)] \quad (2.1)$$

Where SA denotes the surface area; “t” is the thickness, “w” and “l” are the width and length and “h” is the diameter of the drilled round hole. The result of the dimensions and surface area measurement is tabulated in the Table 4. Each sample was measured for its initial mass before being sent into the different tests of oxidation, oxidation continued with metal dusting, and metal dusting test. The initial masses are listed in Table 5.

Table 4. Samples' dimensions and calculated surface area

	Dimensions (cm)				
Sample	w	l	t	h	SA (cm^2)
A1	0.594	1.339	0.139	0.10	1.4998
A2	0.650	1.324	0.136	0.10	1.6298
B1	0.646	1.383	0.138	0.10	1.7185
B2	0.635	1.334	0.143	0.10	1.6290
C1	0.582	1.250	0.136	0.15	1.0108
C2	0.629	1.399	0.129	0.15	1.3407
D1	0.652	1.241	0.138	0.10	1.5124
D2	0.645	1.247	0.147	0.10	1.5366
E1	0.618	1.220	0.140	0.10	1.3942
E2	0.570	1.048	0.147	0.10	1.0421
A3	0.645	1.297	0.140	0.10	1.5885
A4	0.585	1.382	0.140	0.10	1.5393
B3	0.618	1.331	0.138	0.10	1.5547
B4	0.644	1.352	0.131	0.10	1.6360
C3	0.566	1.354	0.136	0.15	1.1124
C4	0.627	1.383	0.134	0.15	1.3304
D3	0.621	1.244	0.137	0.10	1.4277
D4	0.635	1.245	0.141	0.10	1.4829
E3	0.615	1.208	0.146	0.10	1.3898
E4	0.570	1.213	0.148	0.10	1.2822
A5	0.570	1.360	0.139	0.10	1.4586
A6	0.678	1.320	0.136	0.10	1.7050
B5	0.668	1.351	0.142	0.10	1.7500
B6	0.658	1.457	0.139	0.10	1.8770
C5	0.636	1.480	0.138	0.15	1.5240
C6	0.619	1.328	0.134	0.15	1.2233
D5	0.595	1.250	0.138	0.10	1.3684
D6	0.709	1.238	0.159	0.10	1.7463
E5	0.583	1.119	0.144	0.10	1.1666
E6	0.726	1.180	0.151	0.10	1.6606

Table 5. Mass of samples measured prior to the tests

Test Type	Conditions									
Oxidation Test	TEMP (°C)	TIME (h)								
	950	30								
Samples	A1	A2	B1	B2	C1	C2	D1	D2	E1	E2
Initial mass(mg)	842.35	882.69	932.62	898.58	698.22	828.28	779.82	806.86	728.72	586.68
Oxidation Test	TEMP (°C)	TIME (h)	Metal dusting Test	TEMP (°C)	TIME (h)					
	950	30		650	500					
Samples	A3	A4	B3	B4	C3	C4	D3	D4	E3	E4
Initial mass(mg)	858.76	844.73	839.44	848.65	710.2	842.73	748.31	787.79	728.85	727.88
Metal dusting Test	TEMP (°C)	TIME (h)								
	650	500								
Samples	A5	A6	B5	B6	C5	C6	D5	D6	E5	E6
Initial mass(mg)	817.39	919.37	971.17	971.65	915.25	800.19	735.12	1025.04	645.93	864.29

2.4 Oxidation test

The purpose of the oxidation procedure was to develop a known and controlled

distribution of oxide on the specimen surface and to prepare oxidized samples for the metal dusting test to observe performance relative to non-pre-oxidized samples. The oxidation apparatus as shown in Figure 11 was designed so that temperatures of up to 1000 °C can be achieved in the furnace, while steam is constantly flowed throughout the chamber. A quartz rack was built as a specimen holder to hold and hang the testing samples using platinum hang-down wires. Platinum wire is a noble metal and is highly unreactive. This rack apparatus is shown in Figure 10.

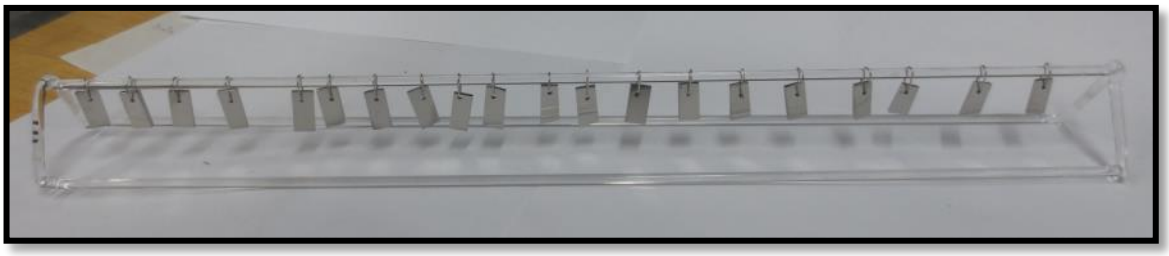

Figure 10. Specimen holder used to suspend the samples when react in the high temperature tube furnace

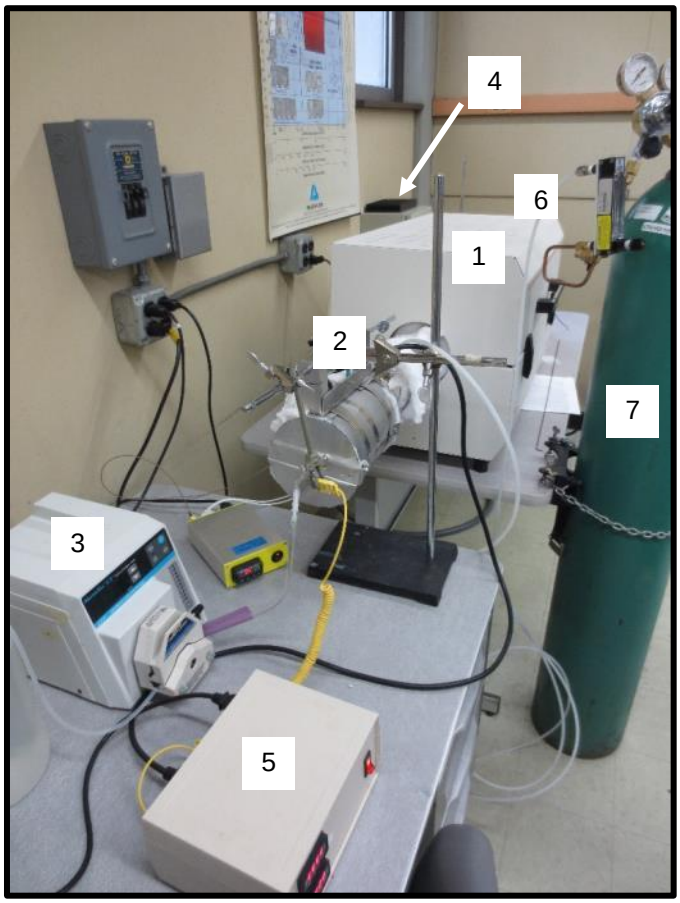

Figure 11. Oxidation apparatus

Features included in the oxidation apparatus are:

1. Tube furnace with quartz 2” tube
2. Water boiler / steam generator
3. Peristatic pump for water flow control
4. Programmable temperature control device
5. Heated inlet and exit regulation unit
6. Heated steam exit
7. Argon used to exhaust other gases and stable the furnace

Steam pre-oxidation was carried out using 100% steam environment as described above,

running for 30 hours at 950 °C.

Figure 12. Illustration of the specimens put in the oxidation apparatus

2.5 Metal dusting test

To construct the metal dusting environment and set up the apparatus, there are few items needed to be considered which include specimen placement, furnace setting, and gas source. Either as-ground samples or post-oxidation samples were hung on the same quartz holder used in the pre-oxidation test and put into the furnace tube for the metal dusting test (as illustrated in Figure 13).

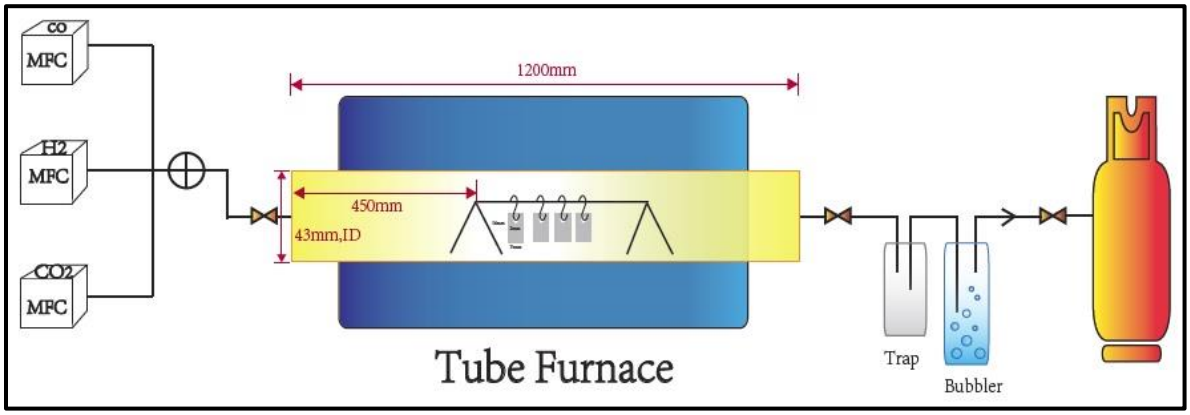

Figure 13. Scheme of the metal dusting test furnace used
MFC: Mass flow controller

The carbon activity in the environment is determined based on the gaseous species of CO, H_2, CO_2 and, based on (1.3) assumed dominant reaction. The gas composition is 45%CO - 50%H_2 – 5% CO_2 at atmospheric pressure of 1 atm in the total flow rate of 300 cc/min.

The carbon activity in the environment could be calculated from reaction (1.3):

$$a_c = (e^{-\frac{\Delta G}{RT}}) \frac{P_{co}^2}{P_{CO2}} \qquad (1.6)$$

where:
$\triangle G$ is the Gibbs energy change
T is the temperature of the system
R is the gas constant
Pi is the partial pressure
a_c will be the carbon activity in the gaseous environment

The carbon activity of the system was therefore being calculated to be 10, which meet the basic criteria of $a_c > 1$ for metal dusting to occur.

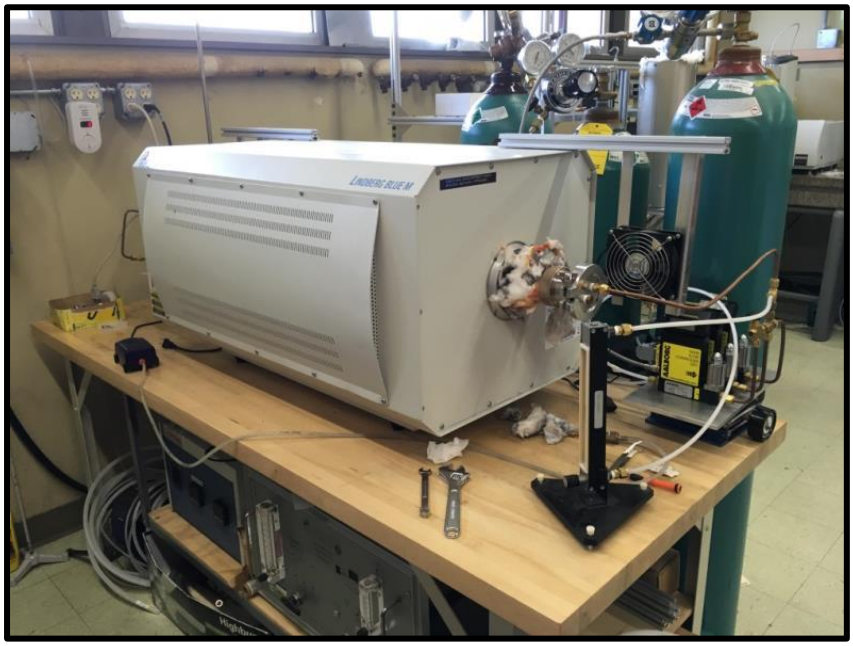

Figure 14. Metal dusting test apparatus

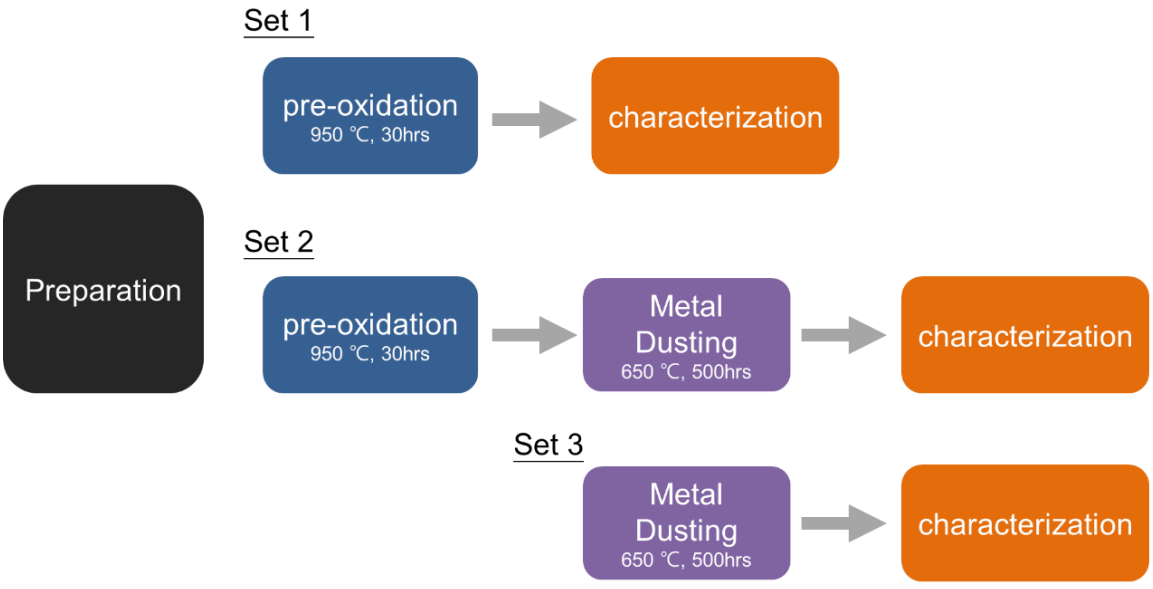

Figure 15. The overview of the testing sets run in this experiment

2.6 Characterization

Samples were characterized after the experiment sets using electronic balance, optical Stereoscope, Scanning Electron Microscopy (SEM), Energy Dispersive Spectroscopy (EDS), and X-Ray Diffraction (XRD).

2.6.1 Change in mass

Mass measurements before and after exposure were made with a 0.01 mg resolution analytical balance.

2.6.2 Optical Stereoscope

Samples were observed using a Zeiss Stemi 2000-C optical stereoscope for physical changes of raw metal, post-oxidation, and post-metal dusting conditions. This allowed for the observance of any physical appearance changes, such as oxide layer deposition, carbon coherence. In addition, this process allowed for the sub classification of samples based on resulting physical changes.

2.6.3 Scanning Electron Microscopy (SEM)

High magnification images of developed oxide layers, carbon deposition, and metal dusting corrosion of alloys were taken with a JEOL 6460-LV Scanning Electron Microscope to determine the continuity of the oxide layer, severity of carbon deposition and corrosion attack. Images were taken using an accelerating voltage of 15 keV.

2.6.4 Energy Dispersive Spectroscopy (EDS)

In order to identify elemental composition of the oxide layers formed and carbonaceous products. EDS was used. Each EDS scan was to track elemental data for the elements Fe, Cr, Ni, al, O and C as this allowed for interpretation of the beginning of the oxide layer, carbon deposition, any elemental mixtures, and the base metal.

2.6.5 X-Ray Diffraction (XRD)

X-Ray Diffraction was also performed on samples of oxidation treatment and metal dusting treatment to identify if there is signal of oxides and carbon upon the surface of alloys. X-rays are high energy photons (Cu Kα 8.04 KeV, λ = 0.154 nm) with wavelengths (λ) comparable to inter-atomic spacing (d ~ 0.2-0.4 nm).

CHAPTER 3. RESULTS

3.1 Change in mass results

Measuring the mass change of the specimens prior to and after the oxidation and metal dusting tests, we can quantify the performance and understand the structural and surface change by comparing the results with the later microscopic and element identifying results. For those specimens which went through the 30 hours oxidation test, we obtained the results in mass change shown in Figure 16. For the alloy 310, samples gained weights in the range from around 0.58 mg to 0.78 mg per centimeter square area, with mean value of 0.71 mg. For alloy 800H, weights gained in the range from 1.09 mg to 1.12 mg, and a 1.11 mg of mean value. For HP alloy, four specimens' weights abnormally decreased, and from the stereoscope images and later surface characterization it is believed that the partial oxidized layer fell off (spalled) from the alloy's surface when the gas flow in the tube changed or due to the temperature change. The later analysis of the oxide layer formed on the surface of HP alloy were just focused on partial area that covered with oxide layer. For those AFA alloys, the mass gains were uniform and at around 1 mg per centimeter square area.

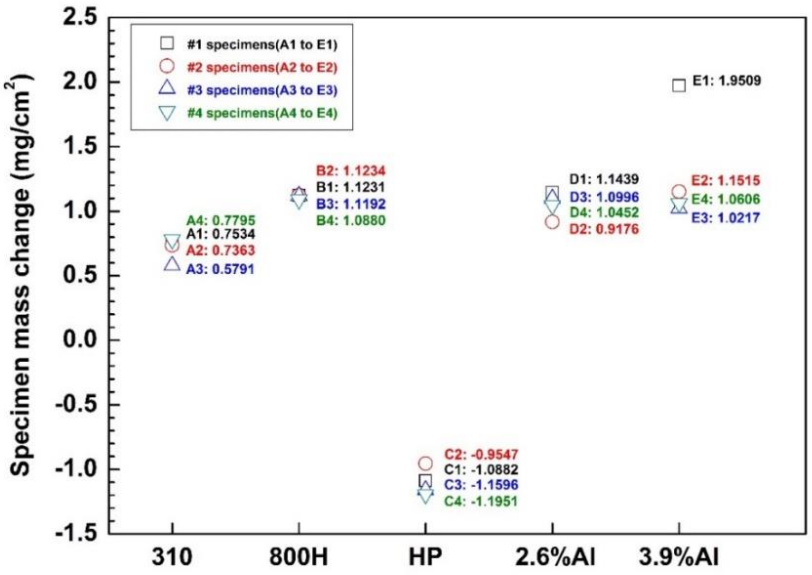

Figure 16. The mass change of alloys of oxidation test (Ox)

Two pieces of each kind of these alloys were used in the metal dusting test after going through the oxidation test to see if there was any specific change and make comparison between each of them. The summarized figure can be seen in Figure 17. Alloy 800H had weight losses of -10.75 mg and -12.73 mg, with mean value of -11.74 mg, which was relatively large, and can be speculated that although carbon deposited on the surface, corrosions to the base alloy occurred and resulted in severe weight losses. For alloy 310, weight lost of -0.04 mg and -0.07 mg, with the mean value close to 0.06 mg indicated that less severe corrosion occurred. For alloy HP, dramatic weight loss of -112.73 mg and -135.04 mg, with the mean value of 123.89 mg, was observed which could indicate severe break off happened to these alloys. In the situations of AFA alloys, there were no weight losses but instead mass gain. 2.6%Al alloys performed a positive mass change of 0.147 mg and 0.148 mg, with mean value close to 0.148 mg, and slightly corrosion of alloys can be predicted. 3.9%Al alloys had mass gains of 6.63 mg and 6.08 mg, with mean value of

6.36 mg, which indicated slightly corrosion or even no corrosion happened to the alloys.

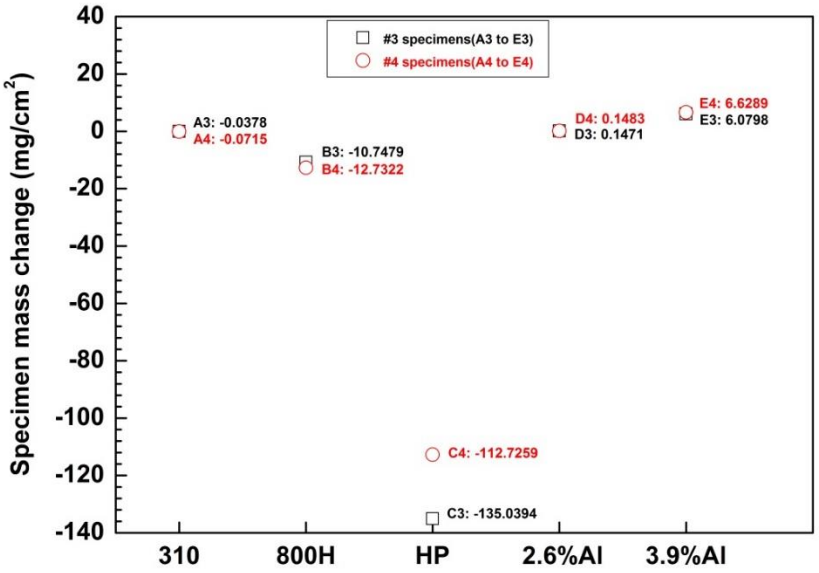

Figure 17.The mass change of alloys after oxidation continued with metal dusting test (Ox+MD)

For solving the concern on the abnormal mass decrease of alloy HP, which were fully covered with carbon in the appearance, attempts were made to tear off the covered carbon with tweezers. The alloy HP was already decomposed into powder of metal carbides and three little pieces of metal covered with carbon as shown in Figure 18 were recovered. Therefore, the dramatical mass losses of alloy HP which were pre-oxidized prior to metal dusting experienced severe decomposition when exposed to this carbonaceous environment.

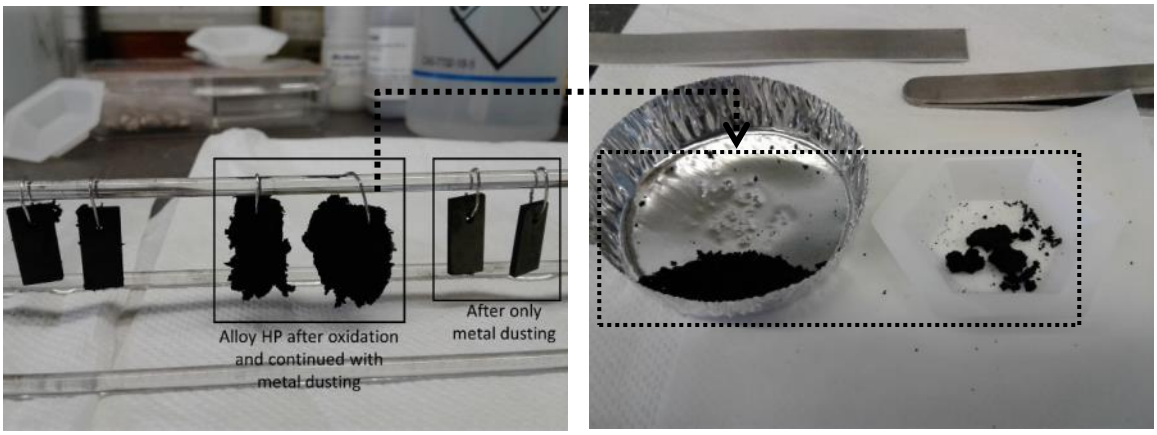

Figure 18.The carbon deposition and removal of alloy HP after oxidation continued with metal dusting test (Ox+MD)

In the other set of test, we exposed the five alloys to only metal dusting environment to make further observation and comparison. These samples were not pre-oxidized in steam prior to dusting tests. It was predicted that carbon deposition and corrosive pits might happen to these alloys when exposed to this environment due to a lack of the protective oxide layer. The mass change data of these metal dusting samples were also tracked and summarized as shown in Figure 19. For alloy 800H, different from other alloys, apparent mass losses of -2.103 mg and -8.439 mg occurred which might indicate much severer corrosion happened. It is not clear why the two samples behaved remarkably differently; no differences in sample handling or exposure were present. Alloy 310, HP and AFA all have mass gain ranging from 0.180 mg to 0.411 mg which could indicate that minor corrosion occurred.

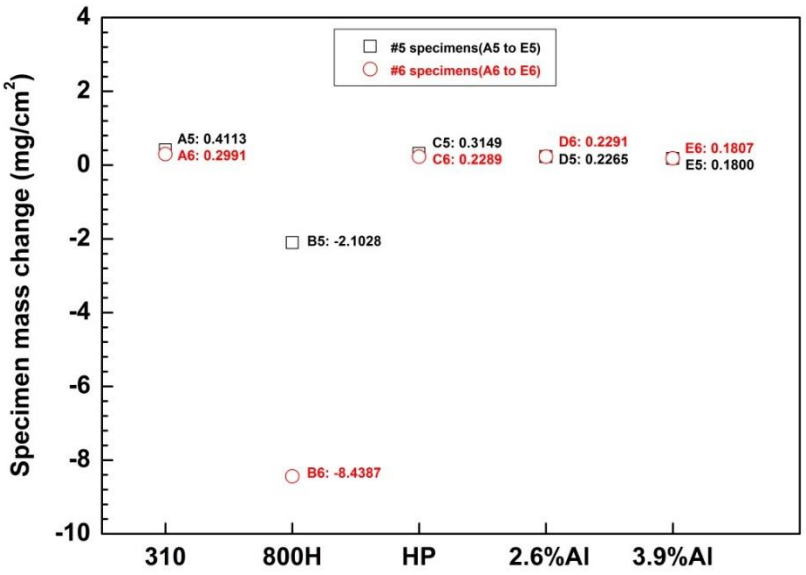

Figure 19.The mass change of alloys after only metal dusting test (MD)

3.2 Optical stereoscope results

All samples were observed for physical appearance and changes for conditions of raw alloy, post oxidation, oxidation continued with metal dusting, and only metal dusting, using a Zeiss Stemi 2000-C optical stereoscope. Lower magnification (x65, 1000μm scale) images were taken to show the broad-view condition of samples being oxidizing or metal dusting treatment (smaller images put on the left side) while higher magnification (x200, 500μm scale) images were taken (larger images put on the right side) for further observe surface oxides, carbon deposition and surface damage to the alloys after exposing the raw alloys to gaseous environment. The illustration of samples that went through oxidation and metal dusting tests are shown in the Figure 20.

From the surface images showed in Figures 21 to Figure 25, we can see that oxides layer covered on the alloys' surface after being exposed to oxidation treatment while there are carbon deposition and scratch-like attacked area on the surface after being exposed to the metal dusting test. The exceptional case is that the alloy HP was nearly destroyed when exposed to metal dusting treatment for 500 hours after the 30h pre-oxidation treatment (Ox+MD), and we can observe tiny metal pieces and carbon filaments from the disintegrated part. The reason why this Ox+MD treating alloy HP teared apart might need further experimental tests such as varying the meal dusting exposure time to shorter amount of time such as 100 hours to observe the sample before it degrades to this extent. The further tests of this alloys were consider as future works.

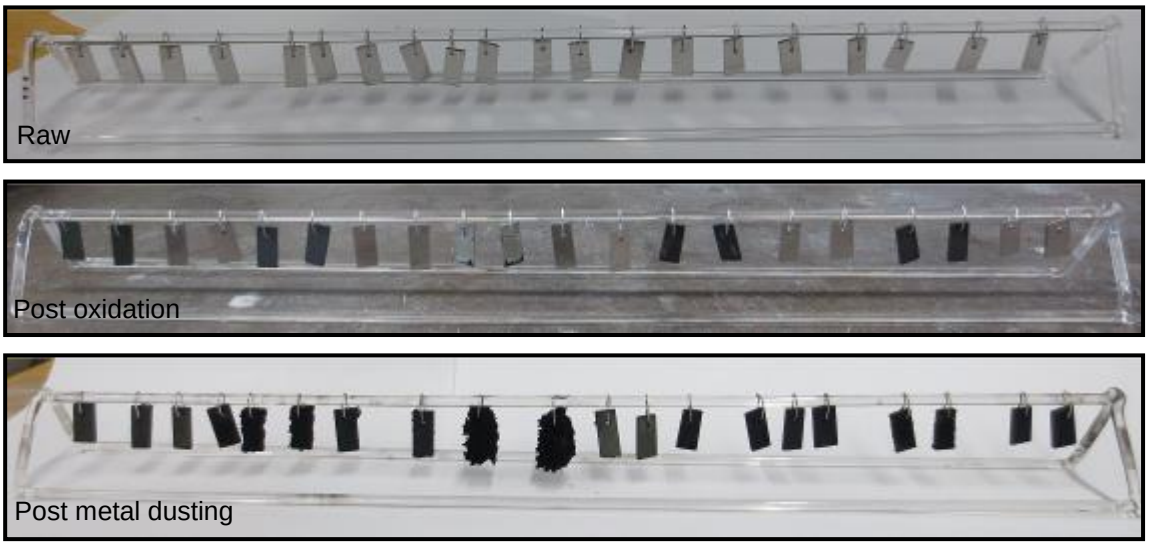

Figure 20. Samples appearance in different stages- raw, post oxidation process, and post metal dusting

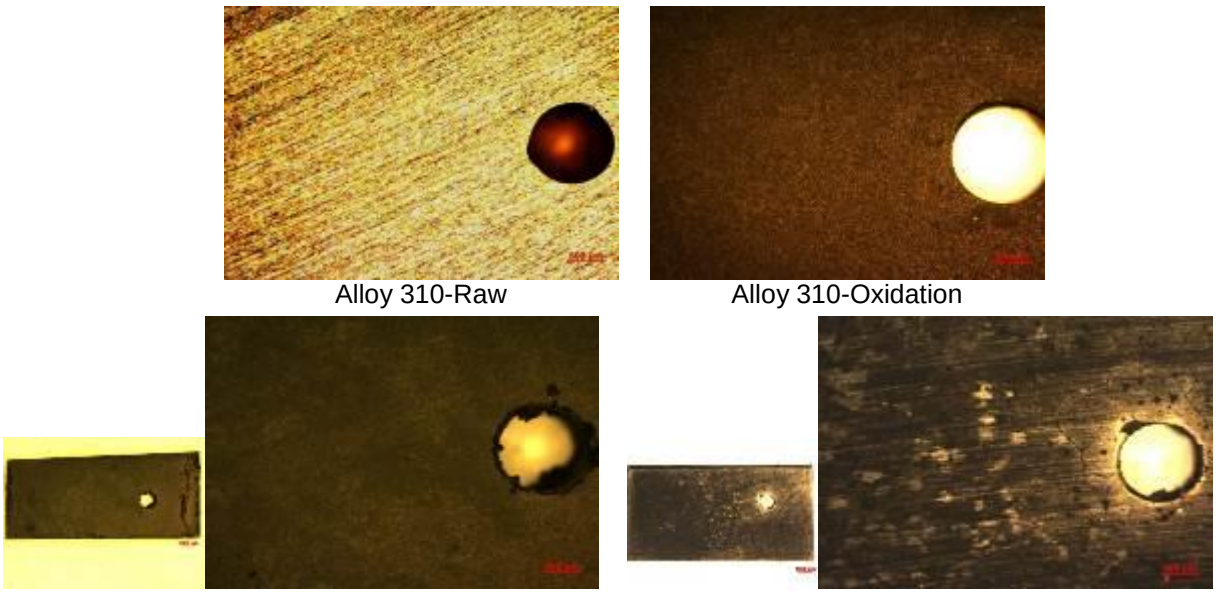

Figure 21. Optical stereoscope images of alloy 310 underwent oxidation and metal dusting tests, 500 µm scale

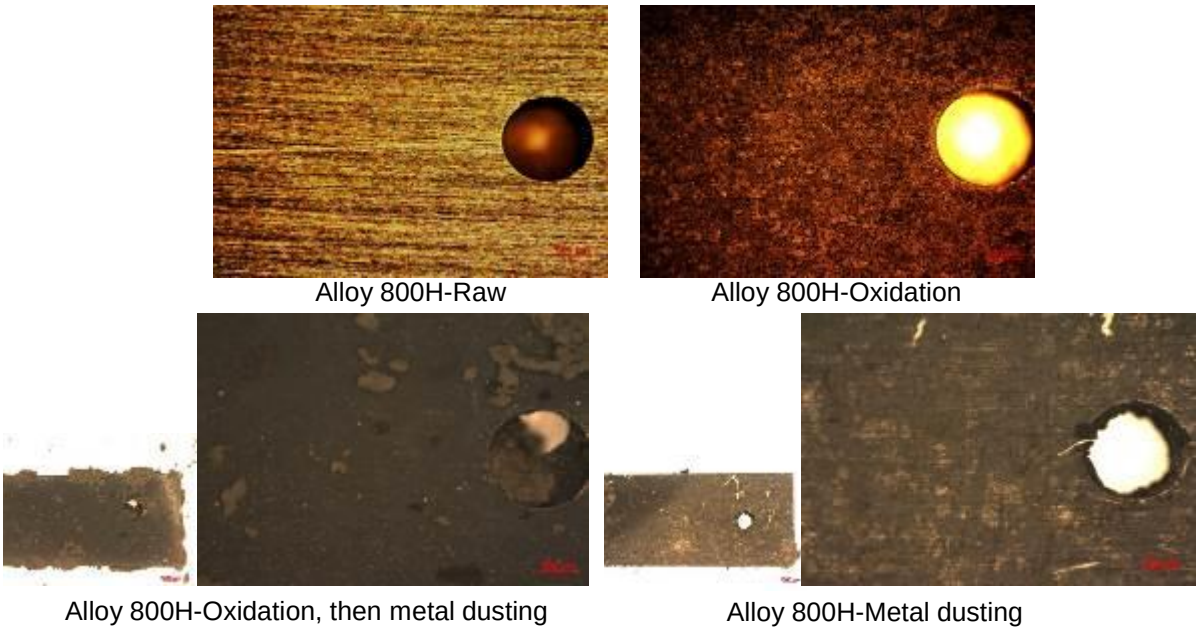

Figure 22. Optical stereoscope images of alloy 800H underwent oxidation and metal dusting tests, 500 µm scale

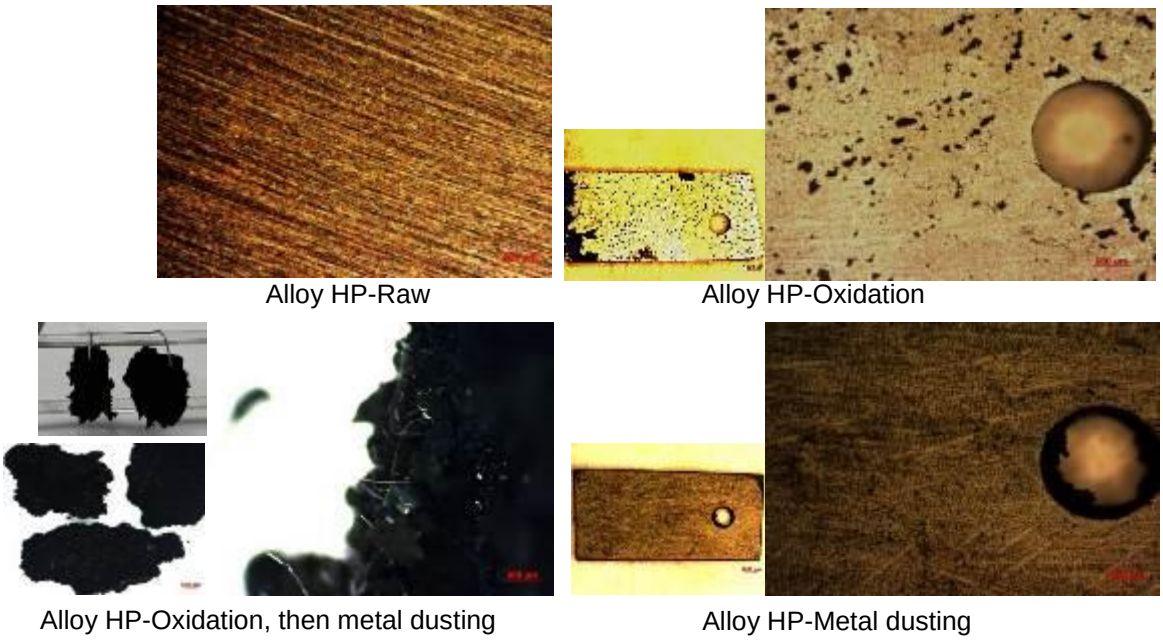

Figure 23. Optical stereoscope images of alloy HP underwent oxidation and metal dusting tests, 500 µm scale

Alloy 2.6%Al-Raw

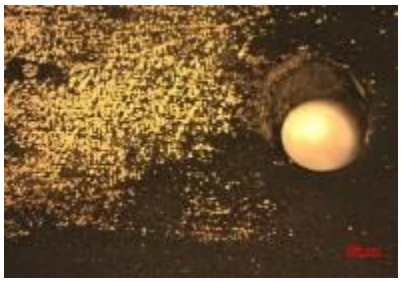

Alloy 2.6%Al-Oxidation

Alloy 2.6%Al-Oxidation, then metal dusting

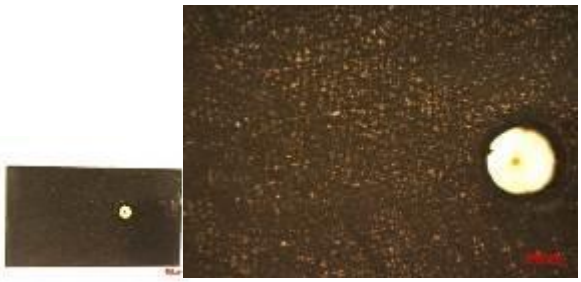

Alloy 2.6%Al-Metal dusting

Figure 24. Optical stereoscope images of alloy 2.6%Al underwent oxidation and metal dusting tests, 500 µm scale

Alloy 3.9%Al-Raw

Alloy 3.9%Al-Oxidation

Alloy 3.9%Al-Oxidation, then metal dusting

Alloy 3.9%Al-Metal dusting

Figure 25. Optical stereoscope images of alloy 3.9%Al underwent oxidation and metal dusting tests, 500 µm scale

3.3 SEM results

Each sample was characterized using SEM to identify if there is oxide layer grown on the surface and if there is any internal oxidation happened to the alloys after going through oxidation test (Ox). For the alloys which went through pre-oxidation continued with metal dusting (Ox+MD) and went through only metal dusting (MD), cross-section and top-view SEM images were also captured to observe the variation of oxide layer, carbon deposition, and carbonaceous attacks. The cross-section images of the pure steam oxidation test were shown in the Figure 26. In the cross-section images, we can see that there were apparent oxide layers grown on the surface of each kind of samples with thickness of 2 μm to 3 μm. In addition to the oxide layers, it was observed in the same figure that there is internal oxidation happened to each kind of alloys. For the 310, 800H, and HP, the internal oxidation extend through the grain structure to the deeper area but does not uniformly happen in every place. While the internal oxidation uniformly distribute in the 2.6%Al, and 3.9%Al alloys.

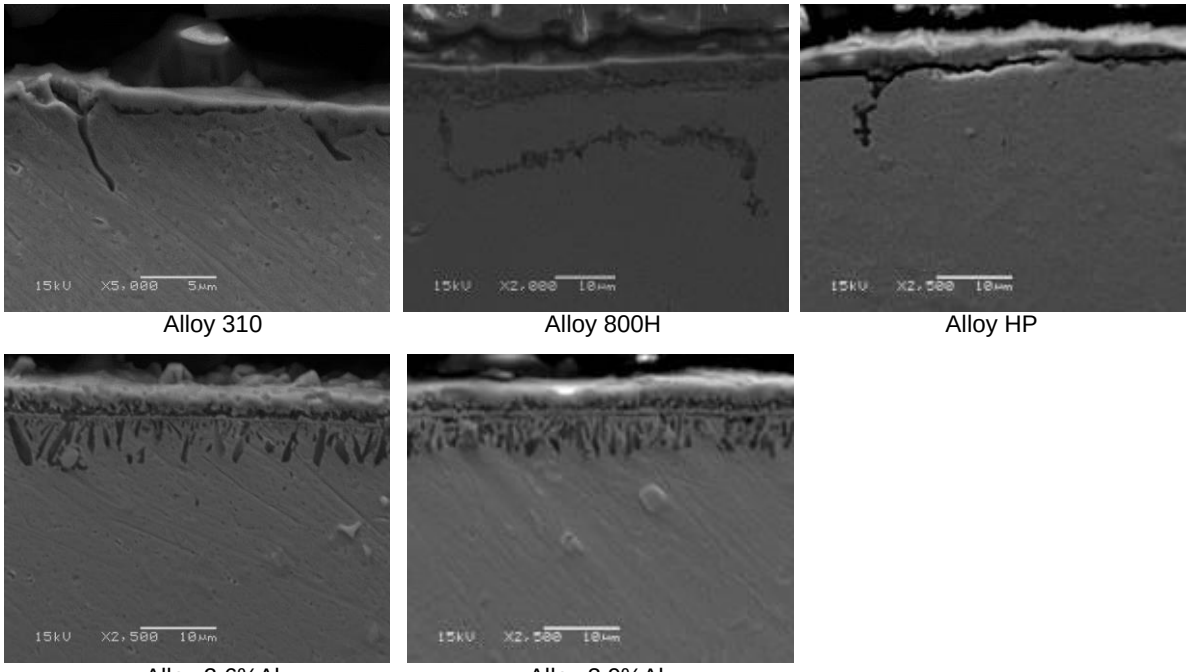

Figure 26. SEM cross-section images of alloys after exposure to pure steam oxidation atmosphere at 950℃ for 30h

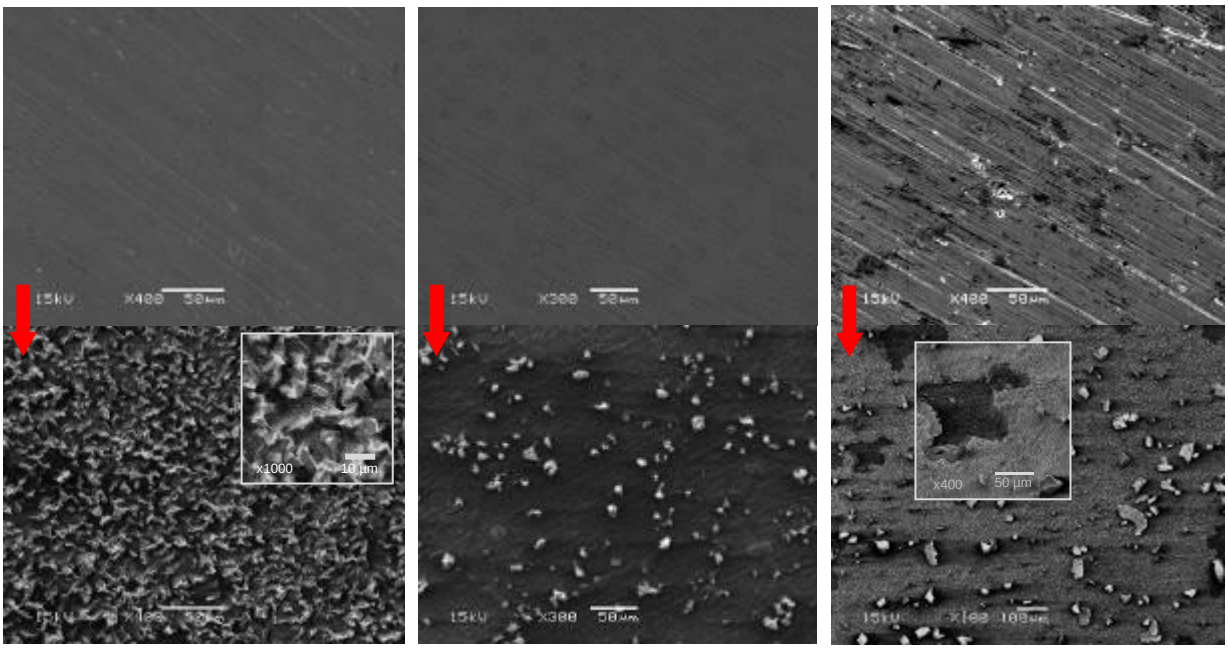

Alloy 310 before and after oxidation | Alloy 800H before and after oxidation | Alloy HP before and after oxidation

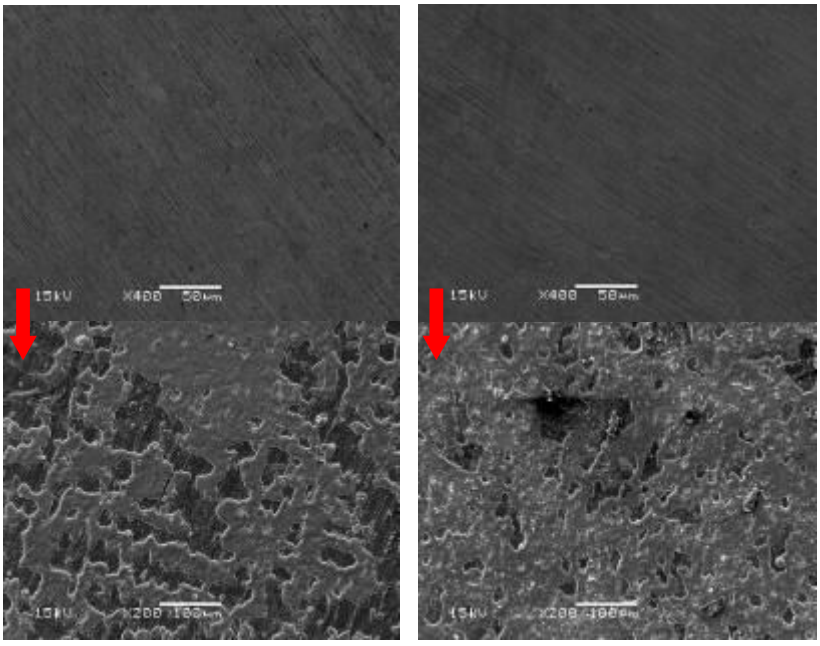

Alloy 2.6%Al before and after oxidation | Alloy 3.9%Al before and after oxidation

Figure 27. SEM top-view images of surface of alloys after exposure to pure steam oxidation atmosphere at 950℃ for 30h

SEM top-view images before and after oxidation were obtained as shown in Figure 27. For alloy 310, after the oxidation treatment, it grew multiple layers of oxide structures. The

layers included a large, plane, and uniform oxide layer with darker color under the microscope observation, which was identified to be chromia later by EDS analysis. Above the darker plane layer, it contained many pillar-shaped, white-colored structures, which were identified to be silicon oxide and manganese dioxide. For 800H, it also grew a uniform plane layer of chromia with white spots above it that were identified to be silicon oxide, manganese dioxide and some titanium dioxide. Upon oxidized HP's surface, large, light grey colored area was formed and later identified to be chromia; while the broken part exposes the darker area which is believed to be bulk material beneath the oxide layer and consisted of mostly iron, nickel, and chromium. For those AFA specimens, which also underwent same oxidized treatment, cloud-shaped oxide layer was formed and later identified to be chromia and alumina; while the darker area beneath it was identified to be internal oxide layer full of alumina in the shallow region of the bulk material.

The top-view images of samples which went through oxidation treatment and continued with metal dusting treatment (Ox+MD) were shown in Figure 28. The pre-oxidized samples were covered with carbon after the metal dusting treatment. For alloy 310 and 800H specimens, there were grouped carbon attached on the oxides layer, and according to the previous mass change results of mass losses, the bulk alloys of these chromia formers were possibly damaged. The cross-section images of these Ox+MD samples were shown in Figure 29. We can see that there were many large pitting holes with the depth close to 500 μm on the alloy 800H, while alloy 310 also got some pitting holes with the depth close to 25 μm. For AFA alloys, there were no apparent pitting holes and some area of oxide layer were damaged slightly due to exposure to metal dusting environment. There were also some holes of nodule appeared in the internal oxidized area of both 2.6%Al alloy and 3.9%Al alloy, and EDS analysis results of line scan were shown in the next section to further

identify the variation of oxide layer and the appearance of internal nodules.

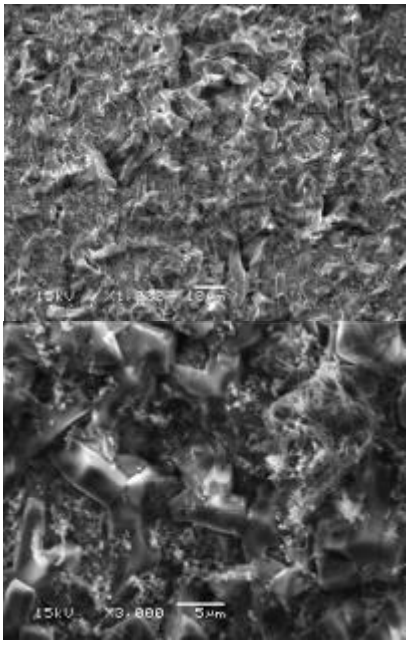

Alloy 310 Ox+MD test

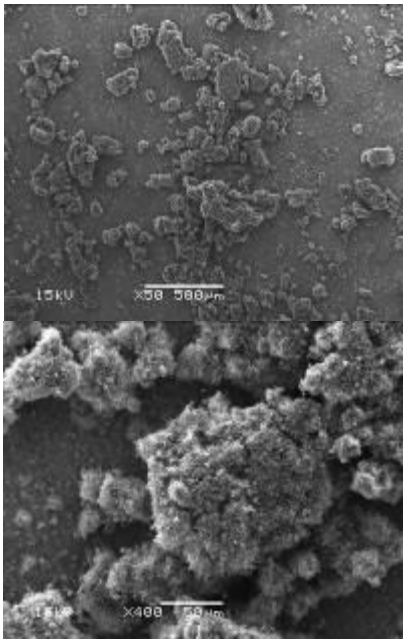

Alloy 800H Ox+MD test

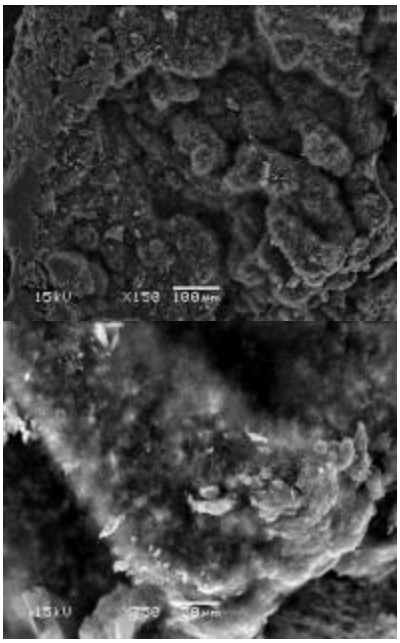

Alloy HP Ox+MD test

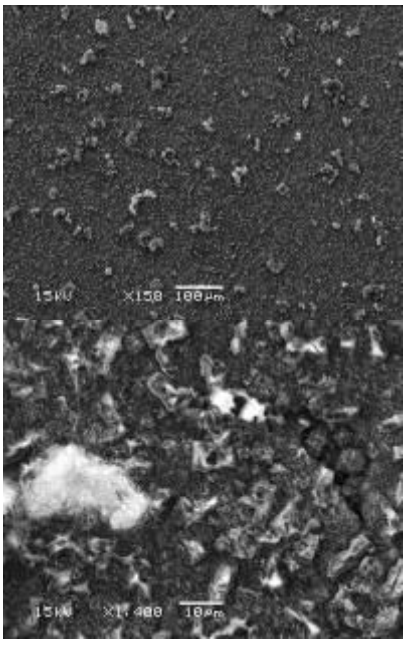

Alloy 2.6%Al Ox+MD test

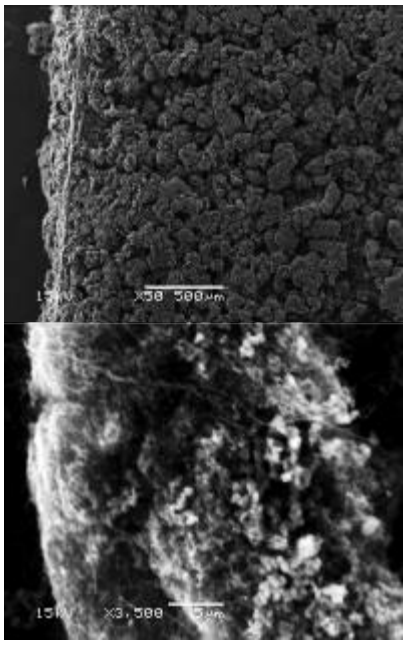

Alloy 3.9%Al Ox+MD test

Figure 28. SEM top-view images of surface of alloys after exposure to oxidation continued with metal dusting test (Ox+MD), lower magnification (up) and higher magnification (down) images

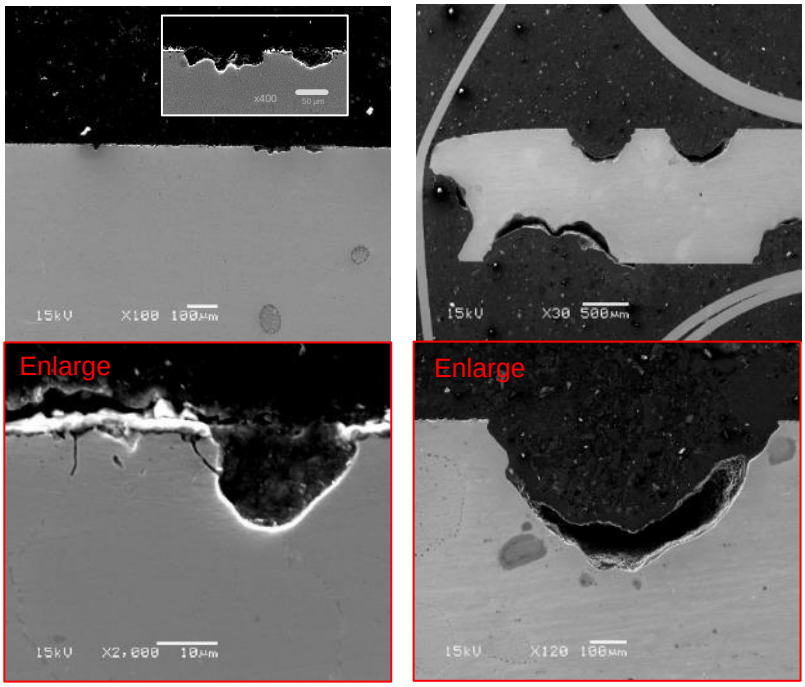

Alloy 310 Ox+MD test

Alloy 800H Ox+MD test

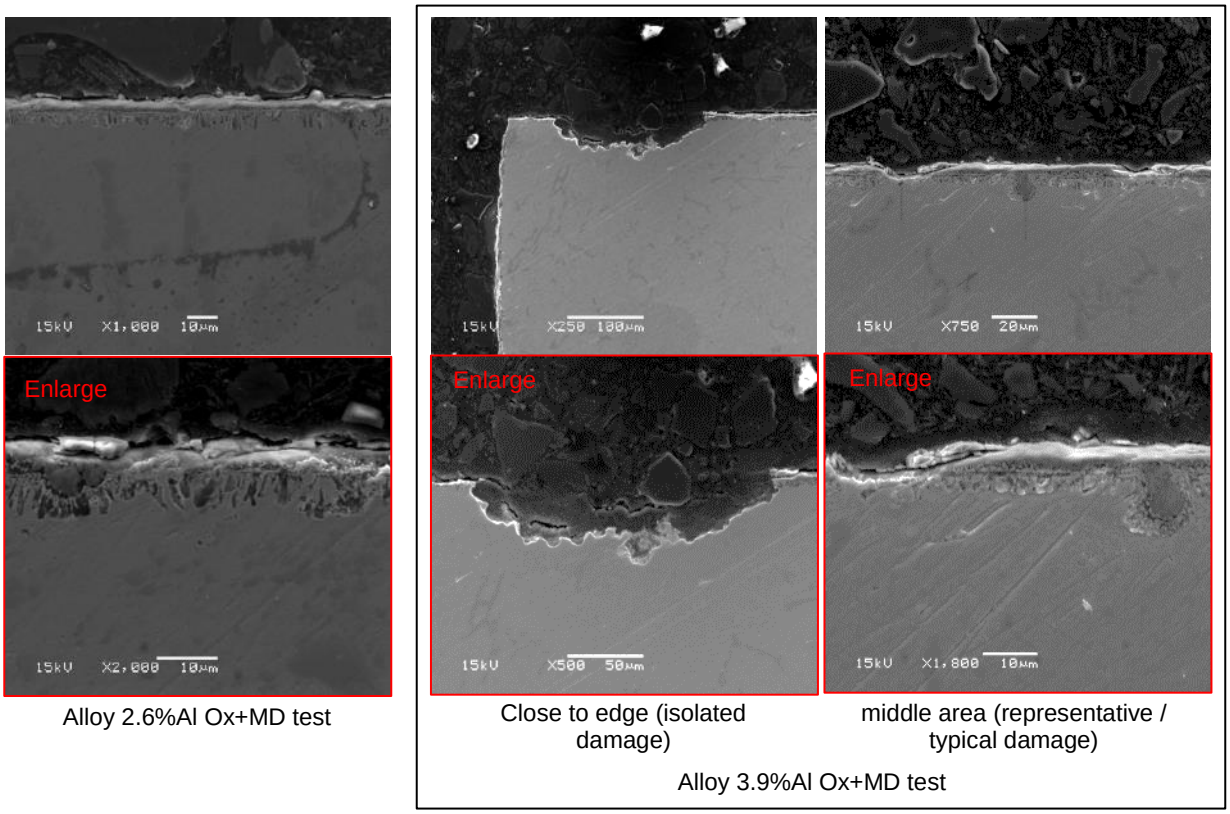

Alloy 2.6%Al Ox+MD test

Close to edge (isolated damage)

middle area (representative / typical damage)

Alloy 3.9%Al Ox+MD test

Figure 29. SEM cross-section images of surface of alloys after exposure to oxidation continued with metal dusting test (Ox+MD), lower magnification (up) and higher magnification (down) images

The SEM top-view images and cross-section view images for the specimens that only went through metal dusting (MD) were also obtained and shown in Figure 30 and Figure 31 relatively. While Figure 32 showed the top-view images after removing the carbon deposited on the surface through ultrasonic clean with acetone. In the Figure 30, we can observe that alloy 800H corroded severely and a large pitting hole appeared at the corner of the alloy and was covered with carbon. Alloy 310 only contained some smaller pits filled with carbon deposits. On the HP alloy surface, there was some carbon deposition but no apparent pitting holes were identified, while for the AFA alloys there was only carbon deposition following the general cast structure of the alloy. In the Figure 31 of the cross-section images of specimens exposed to metal dusting reaction, we can see that there was a large pitting hole formed on alloy 800H which was consistent with our expectation and observation, while there were some smaller pitting holes happened to alloy 310 but not as severe as alloy 800H, and small corroded damages also happened to alloy HP and 2.6%Al alloy, but almost no damages happened to the 3.9%Al alloy. These demonstrate the better resistance to the metal dusting of high-chromium content alloys and aluminum content AFA alloys. The samples were further cleaned with the ultrasonic cleaner in acetone for 4 minutes to remove the surface carbon deposition and dried. Top-view images were obtained as shown in Figure 32. There was a large pitting hole on the alloy 800H, and smaller pitting holes for alloy 310 while there were no obvious pitting holes for alloy HP and AFA alloys.

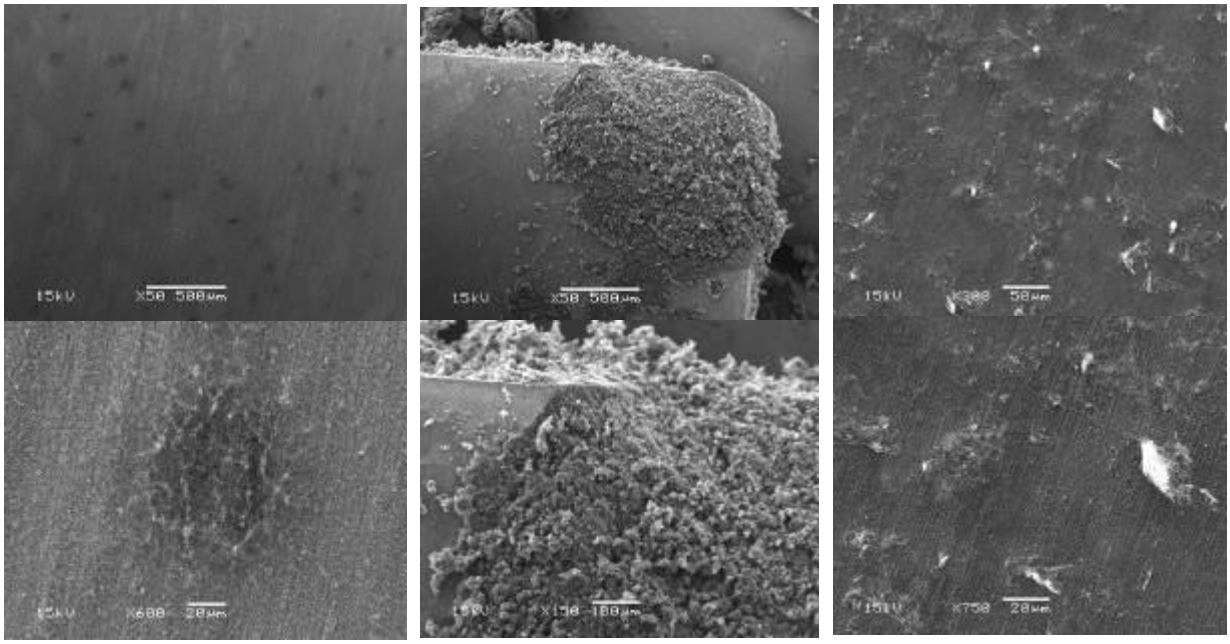

Alloy 310 MD test | Alloy 800H MD test | Alloy HP MD test

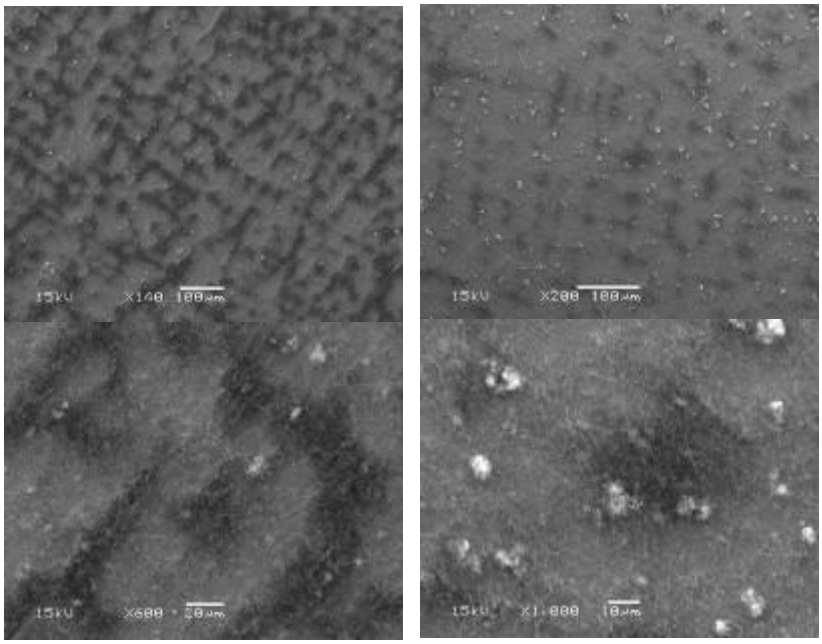

Alloy 2.6%Al MD test | Alloy 3.9%Al MD test

Figure 30. SEM top-view images of surface of alloys after only metal dusting test (MD), lower magnification (up) and higher magnification (down) images

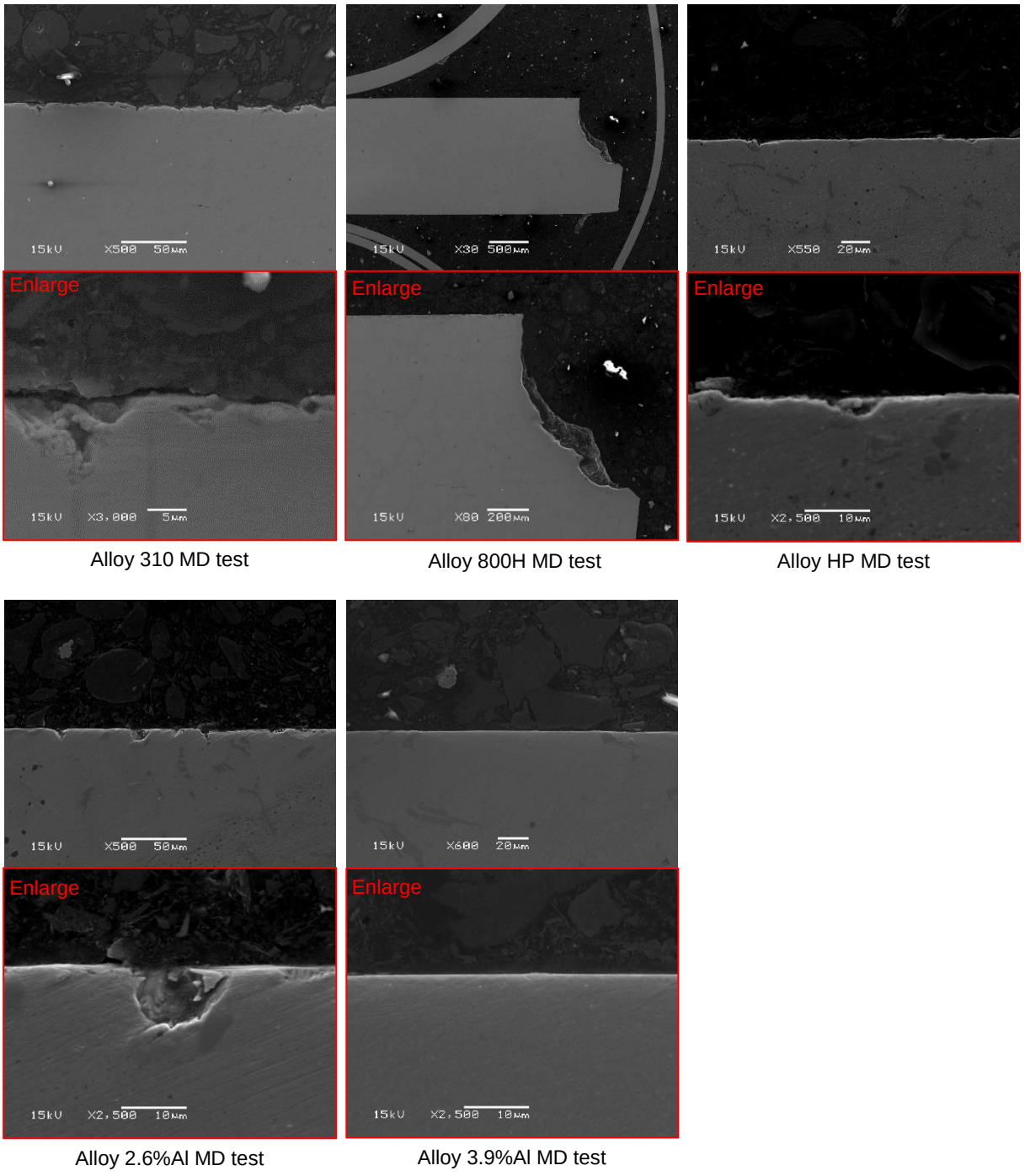

Alloy 310 MD test | Alloy 800H MD test | Alloy HP MD test

Alloy 2.6%Al MD test | Alloy 3.9%Al MD test

Figure 31. SEM cross-section view images of surface of alloys after only metal dusting test (MD), lower magnification (up) and higher magnification (down) images

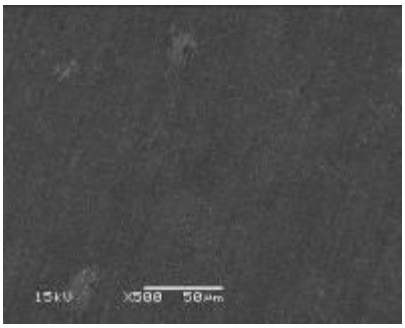

Alloy 310 MD test,
carbon removed

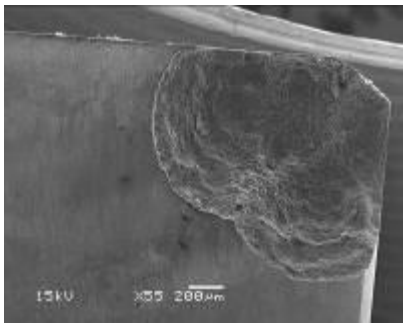

Alloy 800H MD test,
carbon removed

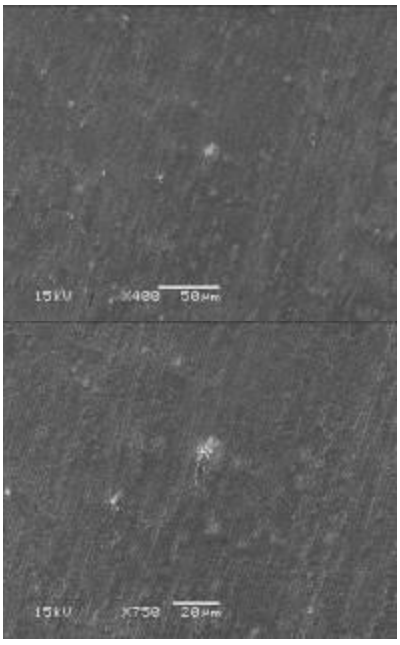

Alloy HP MD test, carbon
removed

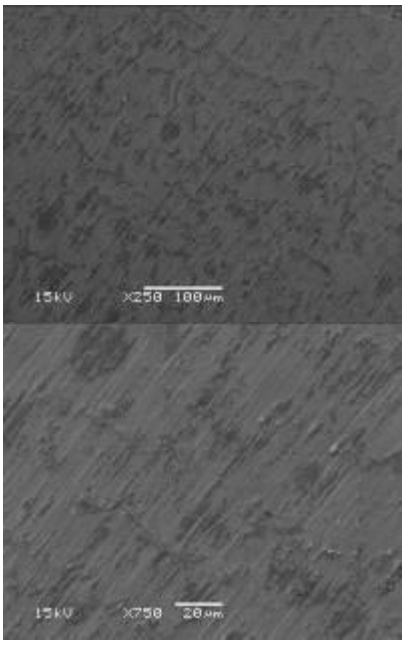

Alloy 2.6%Al MD test,
carbon removed

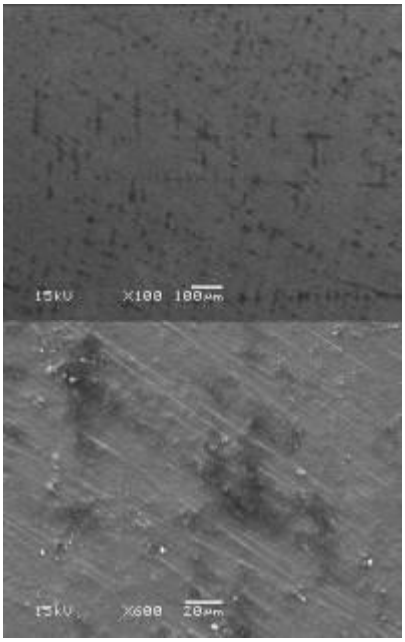

Alloy 3.9%Al MD test,
carbon removed

Figure 32. SEM top-view images of surface of alloys, remove the carbon deposition after only metal dusting test (MD), lower magnification (up) and higher magnification (down) images

3.4 EDS analysis

EDS analysis was used to identify the elemental composition of the oxide layer formed on the surface and the internal oxidation extend under the surface after exposure to oxidation environment. The variation of the oxide layer and the deposition of carbon were also identified for those specimens which went through oxidation test continued with metal dusting test (Ox+MD). For the alloy 310 which was exposed to oxidation environment, the cross-section image analysis are shown in Figure 33 and the top-view image analysis are shown in Figure 38. There was ~1.5 μm thick oxide layer formed on the surface consisted of chromium oxide and a ~8.9 μm deep internal oxidation crack consisted of chromium oxide and silicon oxide in the cross-section images. From the top-view images, there was a layer of chromium oxide covered on the surface and pillar-shaped dots of manganese oxide and silicon oxide scattered upon the chromium oxide layer.

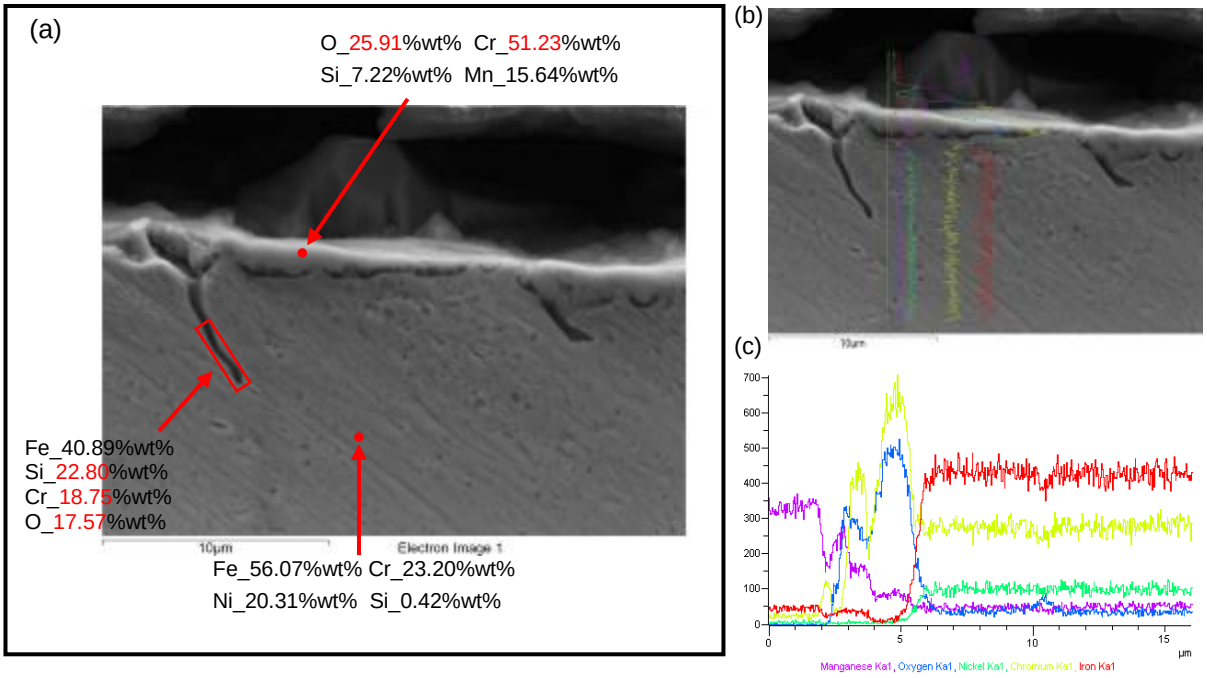

Figure 33. SEM cross-section image of alloy 310 post-oxidation with EDS analysis, (a) spot analysis, (b) and (c) are line scan analysis

For the alloy 800H which was exposed to oxidation environment, the cross-section image

analysis are shown as Figure 34 and the top-view image analysis are shown in Figure 38. There was ~2.7 μm thick oxide layer formed on the surface consisting of chromium oxide and a ~14.2 μm deep internal oxidation crack consisting of aluminum oxide and titanium oxide in the cross-section images. From the top-view images, there were indeed a layer of chromium oxide covered on the surface and pillar-shaped dots of manganese oxide, silicon oxide, and titanium oxide scattered upon the chromium oxide layer.

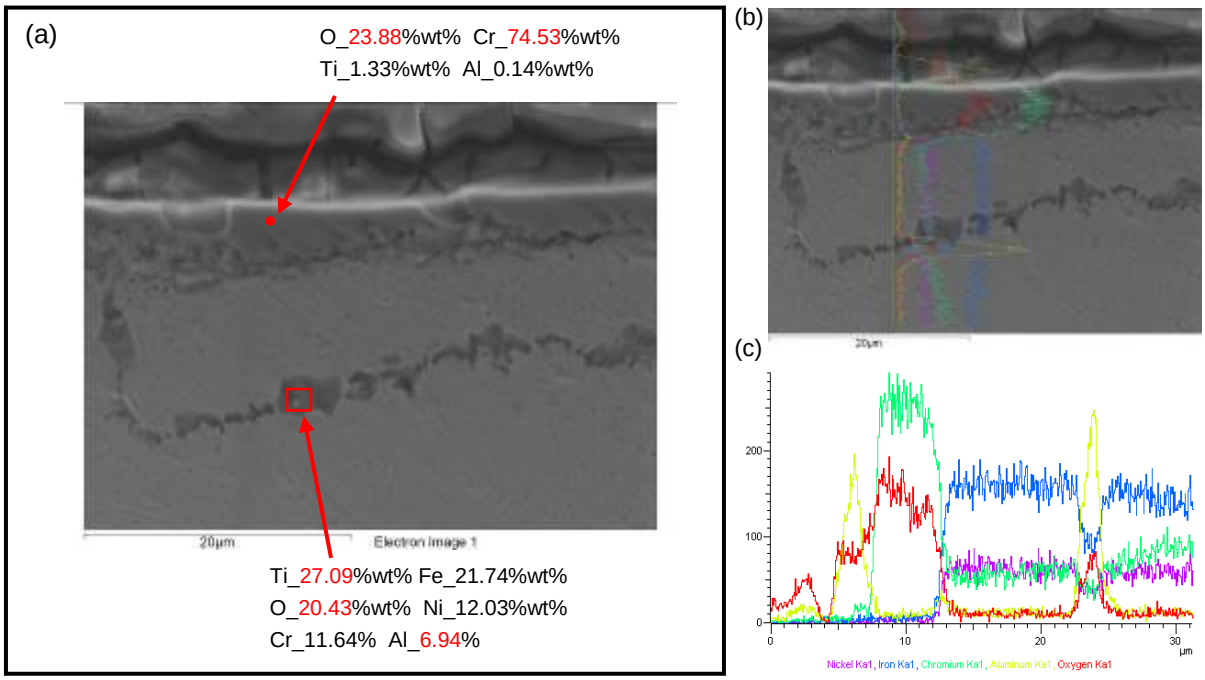

Figure 34. SEM cross-section image of alloy 800H post-oxidation with EDS analysis, (a) spot analysis, (b) and (c) are line scan analysis

For the alloy HP which was exposed to oxidation environment, the cross-section images are shown in Figure 35 and the top-view image analysis are also shown in Figure 38 There was ~2.6 μm thick oxide layer formed on the surface consisting of chromium oxide and a

~8.8 μm deep internal oxidation crack consisting of chromium oxide and some silicon oxide in the cross-section images. From the top-view images, there was a layer of chromium oxide covering on the surface.

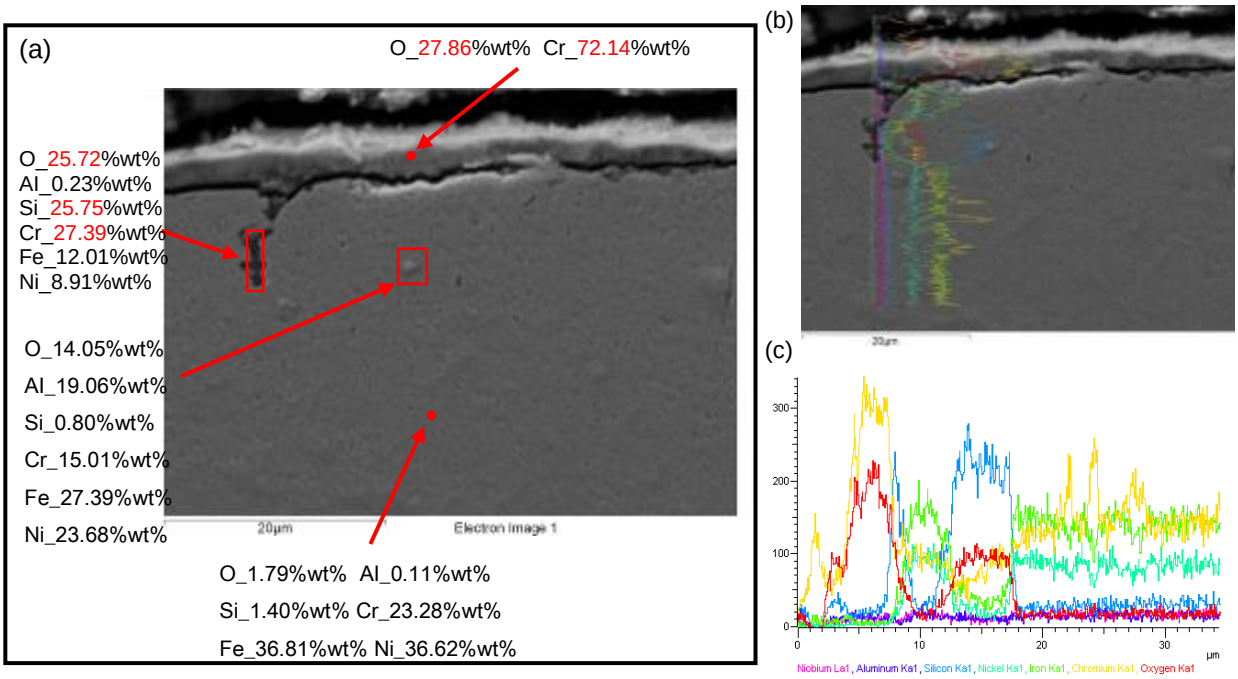

Figure 35. SEM cross-section image of alloy HP post-oxidation with EDS analysis, (a) spot analysis, (b) and (c) are line scan analysis

For the 2.6%Al alloy of AFAs which was exposed to oxidation environment, the cross-section image analysis are shown in Figure 36 and the top-view image analysis are shown in Figure 38. We can observe that there was ~2.8 μm thick oxide layer formed on the surface consisted of chromium oxide and the internal oxidation crack of ~8.5 μm deep consisted of aluminum oxide in the cross-section images. From the top-view images, there

apparently was a layer of chromium oxide covering the surface while the internal area consisted of mostly aluminum oxide and some chromium oxide as internal oxidation.

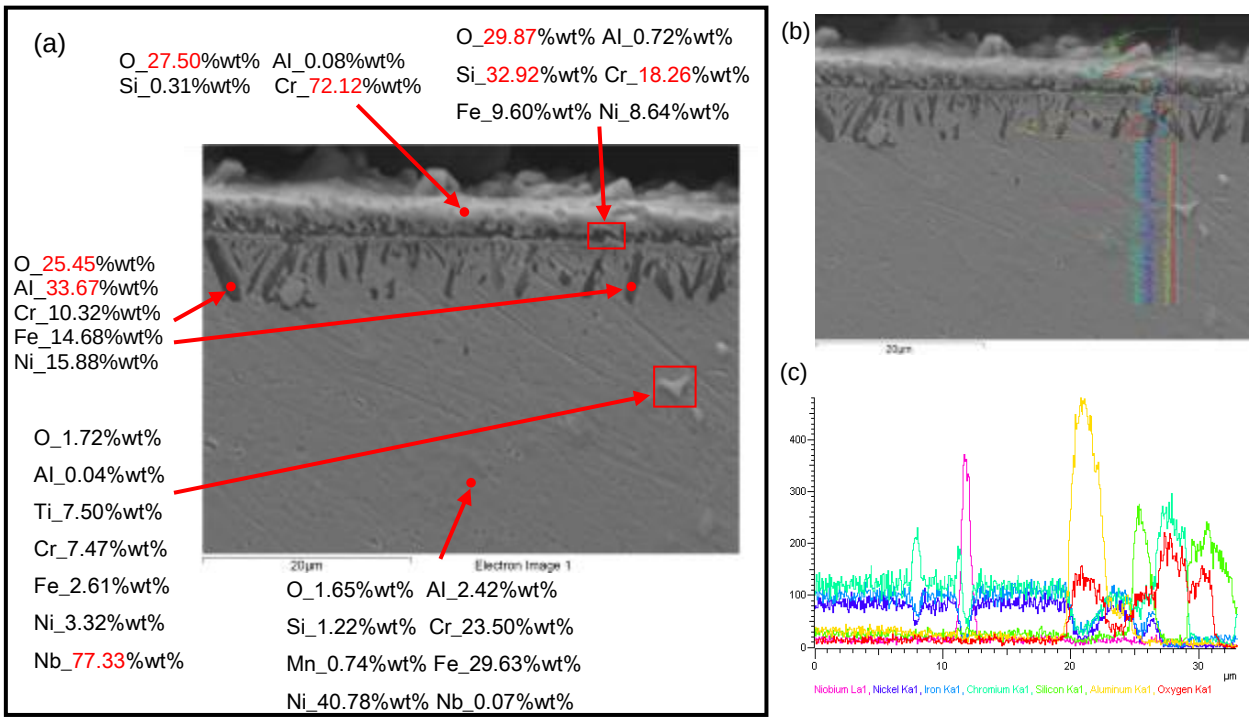

Figure 36. SEM cross-section image of alloy 2.6%Al post-oxidation with EDS analysis, (a) spot analysis, (b) and (c) are line scan analysis

For the 3.9%Al alloy of AFAs which was exposed to oxidation environment, the cross-section image analysis are shown in Figure 37 and the top-view image analysis are also shown in Figure 38. Similar to the 2.6%Al alloy, there was ~2.7 µm thick oxide layer formed on the surface consisting of chromium oxide and shallower internal oxidation cracks ~5.8 µm deep consisting of aluminum oxide. From the top-view images, there was a layer of chromium oxide covered on the surface while the internal area consisted of mostly

aluminum oxide and some chromium oxide as internal oxidation.

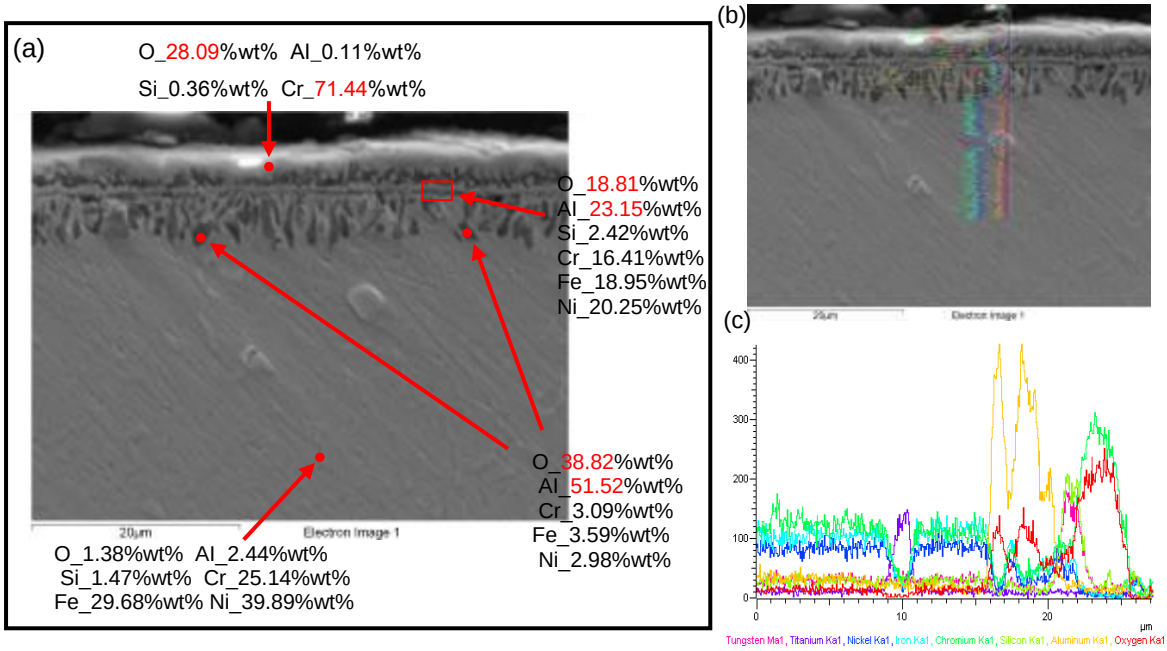

Figure 37. SEM cross-section image of alloy 3.9%Al post-oxidation with EDS analysis, (a) spot analysis, (b) and (c) are line scan analysis

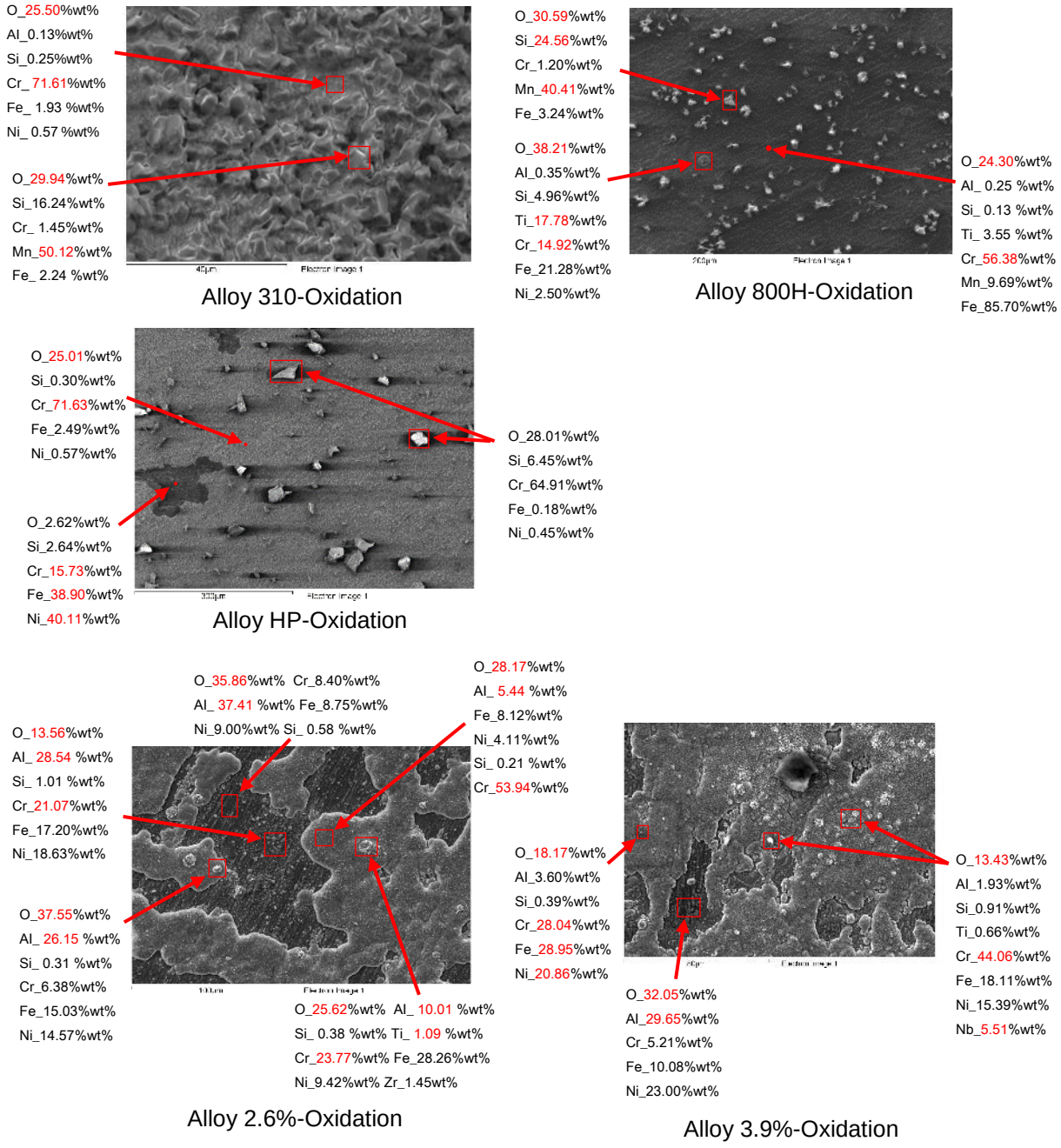

Figure 38. SEM top-view images of alloys post-oxidation with EDS spot and region analysis

In the set of specimens which exposed to oxidation test continued with metal dusting test (Ox+MD). Elemental composition analysis from the cross-section view was performed to observe if there were any variation of the oxide layer, internal oxidation area, and corroded area after exposure to metal dusting environment. For alloy 310, the spot analysis and line scan were completed as shown in Figure 39. There were pitting holes with a depth close to 25 μm formed on the surface. Inside the pitting holes, carbon deposition was detected but no carbide formations such as cementite (Fe_3C) were detected. The line scan on the area of oxide layer aside the pitting hole showed that the thickness of oxide layer might had increased a little bit due to metal dusting reaction, and it could be speculated as the occurring of selective oxidation.

The line scan analysis of the alloy 800H which went through oxidation test continued with metal dusting test (Ox+MD) are shown in Figure 40. The line scan focused on the oxide layer region near the large pitting holes (~500 μm deep) where the oxide layer was damaged but large holes hadn't formed. The distribution of chromium oxide apparently increased, which might represent the corrosion of internal oxidation region or the occurring of selective oxidation.

The line scan images of AFA alloys are shown in Figure 41. From the images, we can see that some regions of oxide layer were corroded. Similar to previous chromia-forming alloys, the line scan results also showed the increase in thickness of oxide layer of chromium oxide. The nodules formed in the internal area consisted of chromia and some alumina was detected, indicating that metal dusting could cause a pitting hole in the internal oxidation area where the structure might be not so stable as the bulk area.

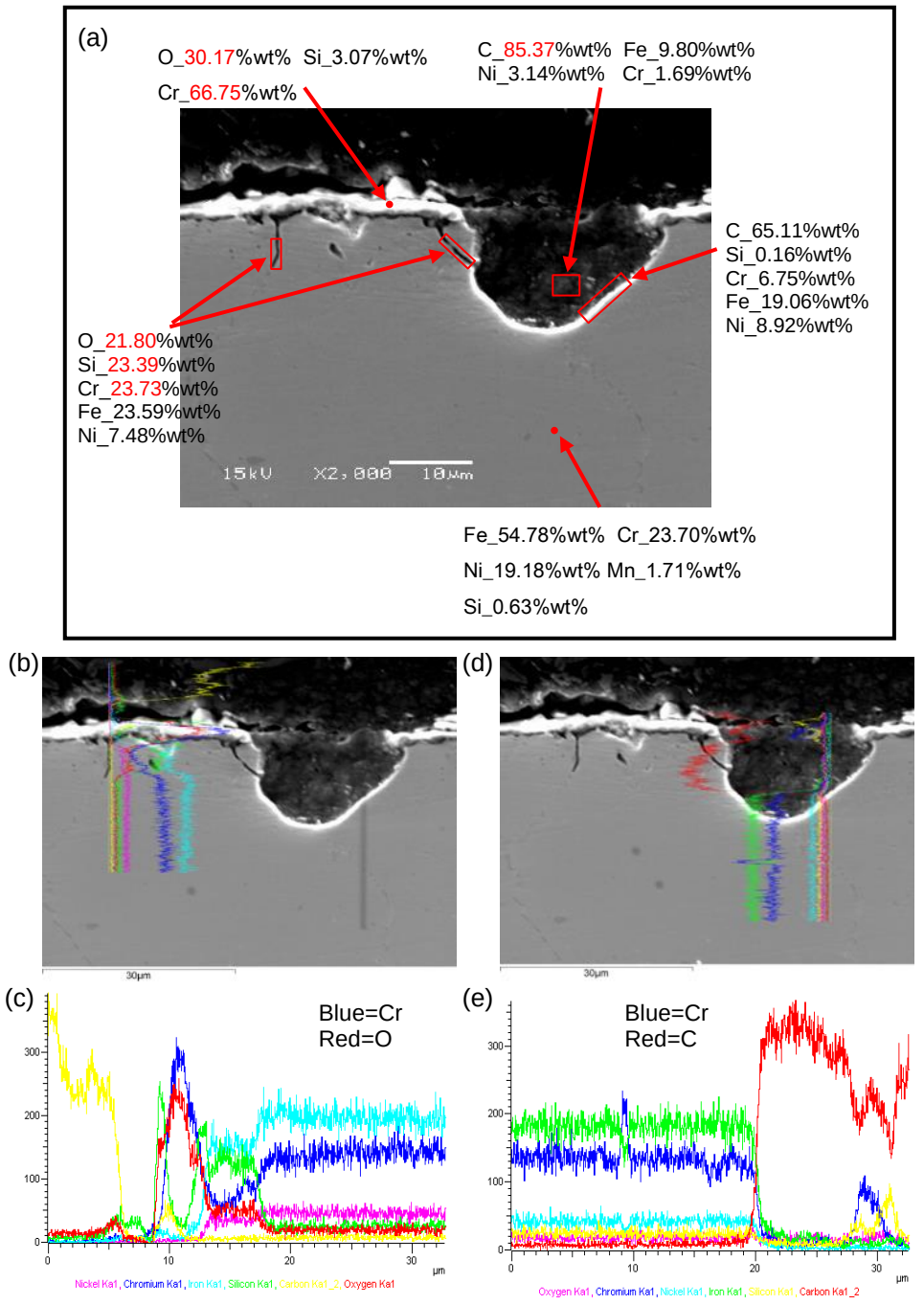

Figure 39. SEM cross-section image of alloy 310 after Ox+MD test with EDS analysis, (a) spot analysis, (b) and (c) are line scan analysis of the oxide layer; while (d) and (e) are line scan of the pit

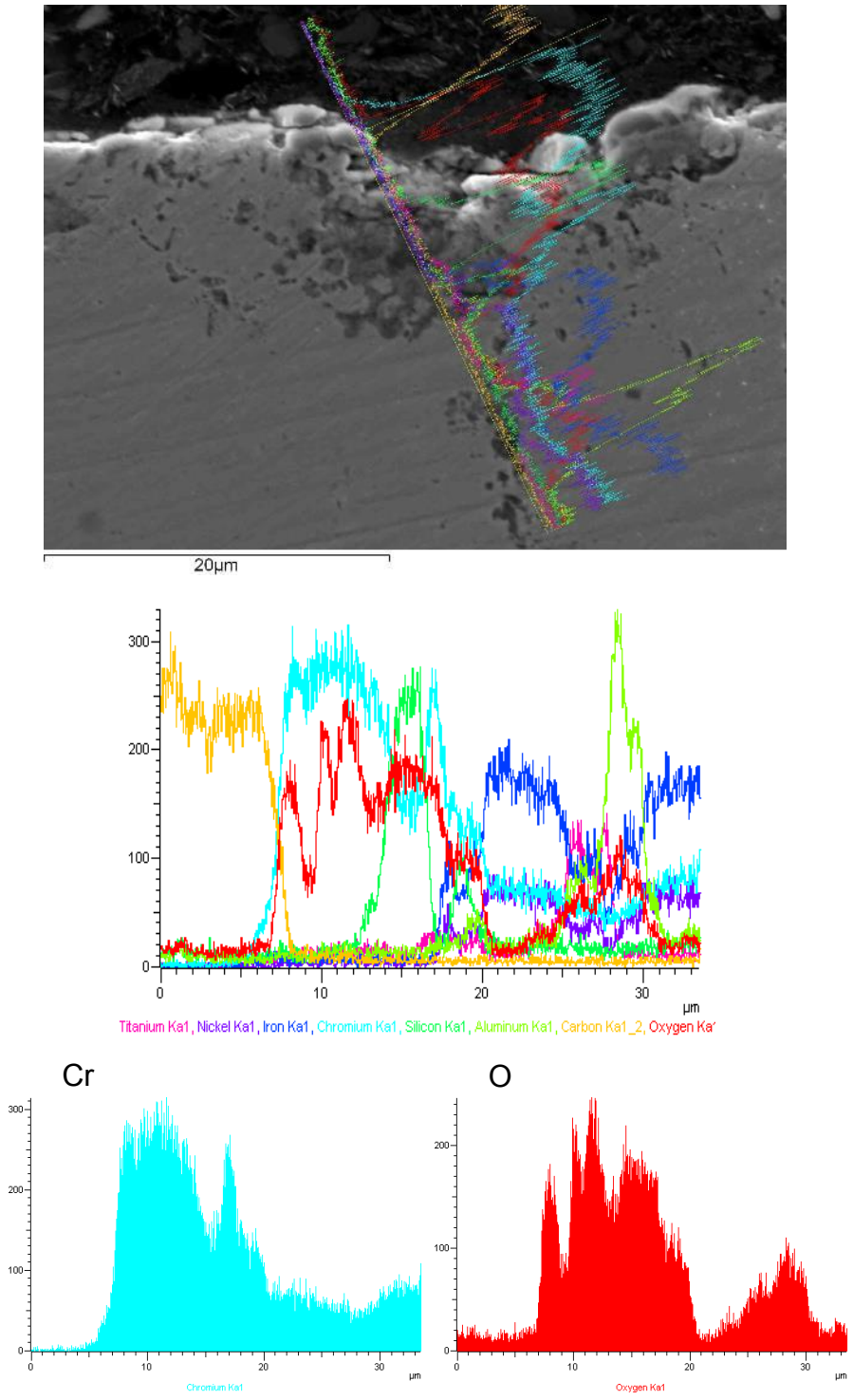

Figure 40. SEM cross-section image of alloy 800H after Ox+MD test with EDS line scan analysis

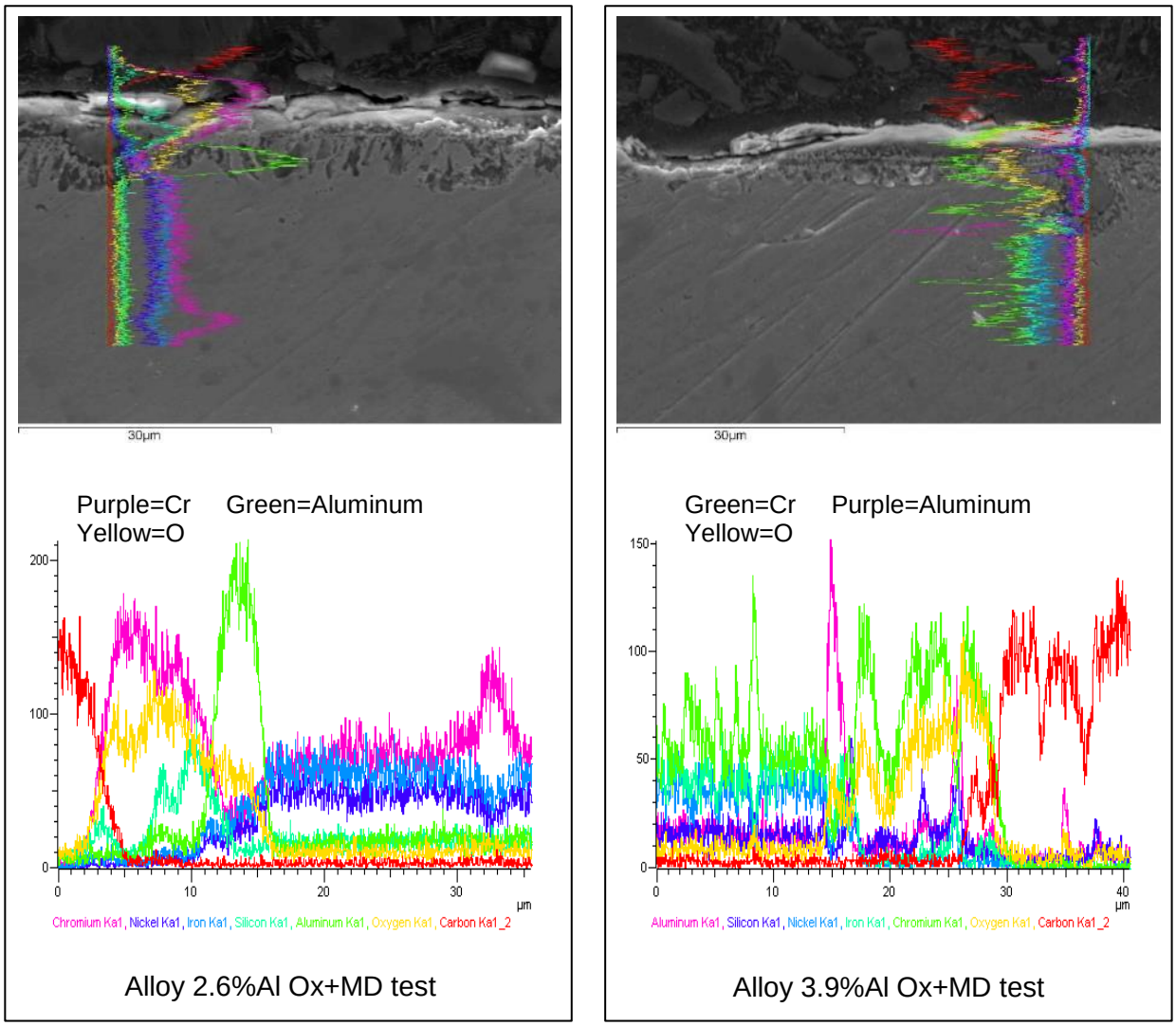

Figure 41. SEM cross-section image of AFA alloys after Ox+MD test with EDS line scan analysis

3.5 XRD analysis

XRD analysis results of two sets of tests: Oxidation test (Ox), and only metal dusting test (MD) were also conducted and shown in Figure 42 and Figure 43. In Figure 42, chromia formed on the alloys' surface while there were some silicon oxides detected on the alloy 310 and alloy 800H. For the AFA alloys, there was detection of alumina that proved the formation and existence of alumina on the surface of AFA alloys after exposed to pure steam oxidation test. In Figure 43 of the specimens which went through only metal dusting, carbon and some graphite were detected upon alloy's surface which indicate the occurring of metal dusting mechanisms.

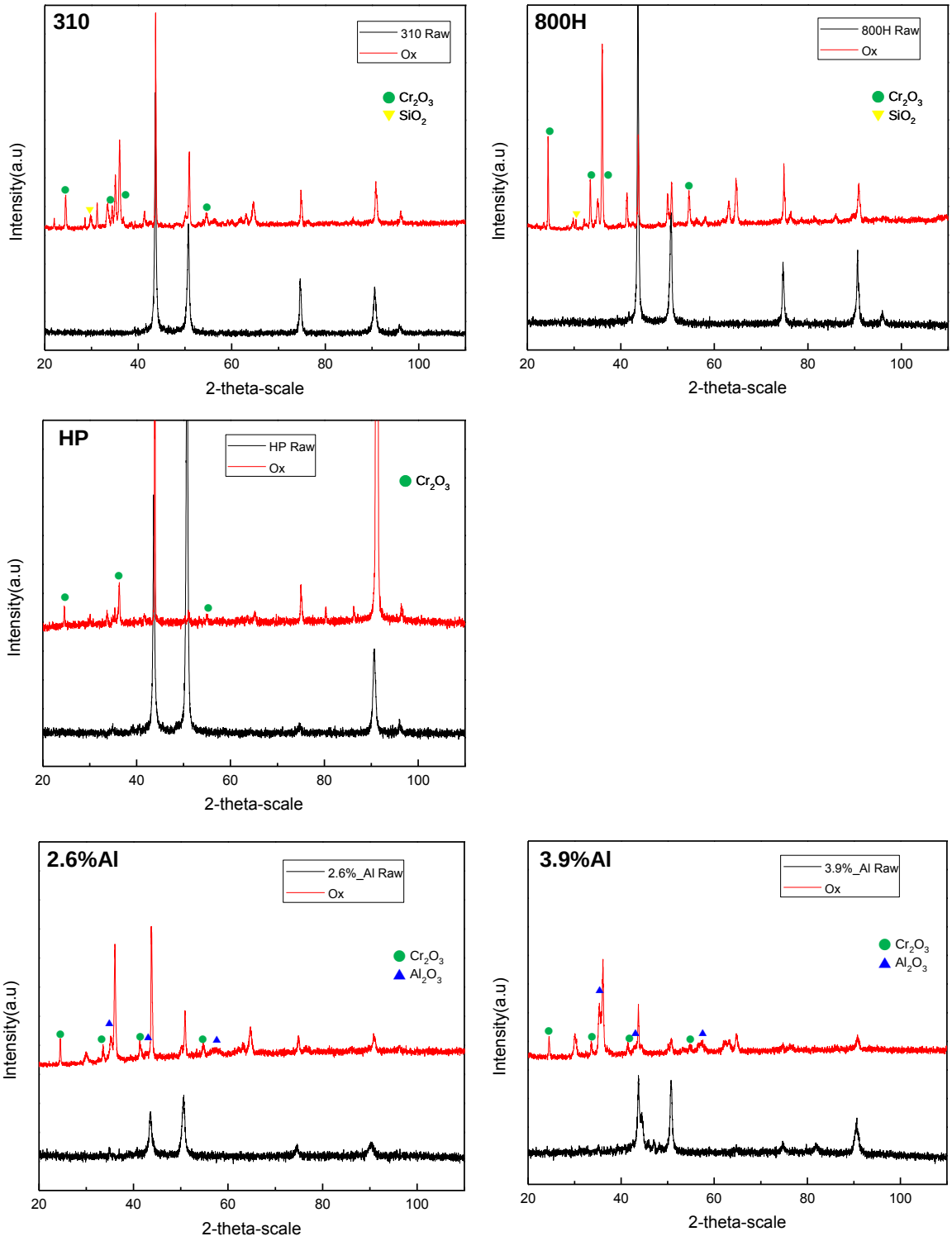

Figure 42. XRD diagrams obtained by analyzing alloys' surface after exposure to oxidation environment (Ox)

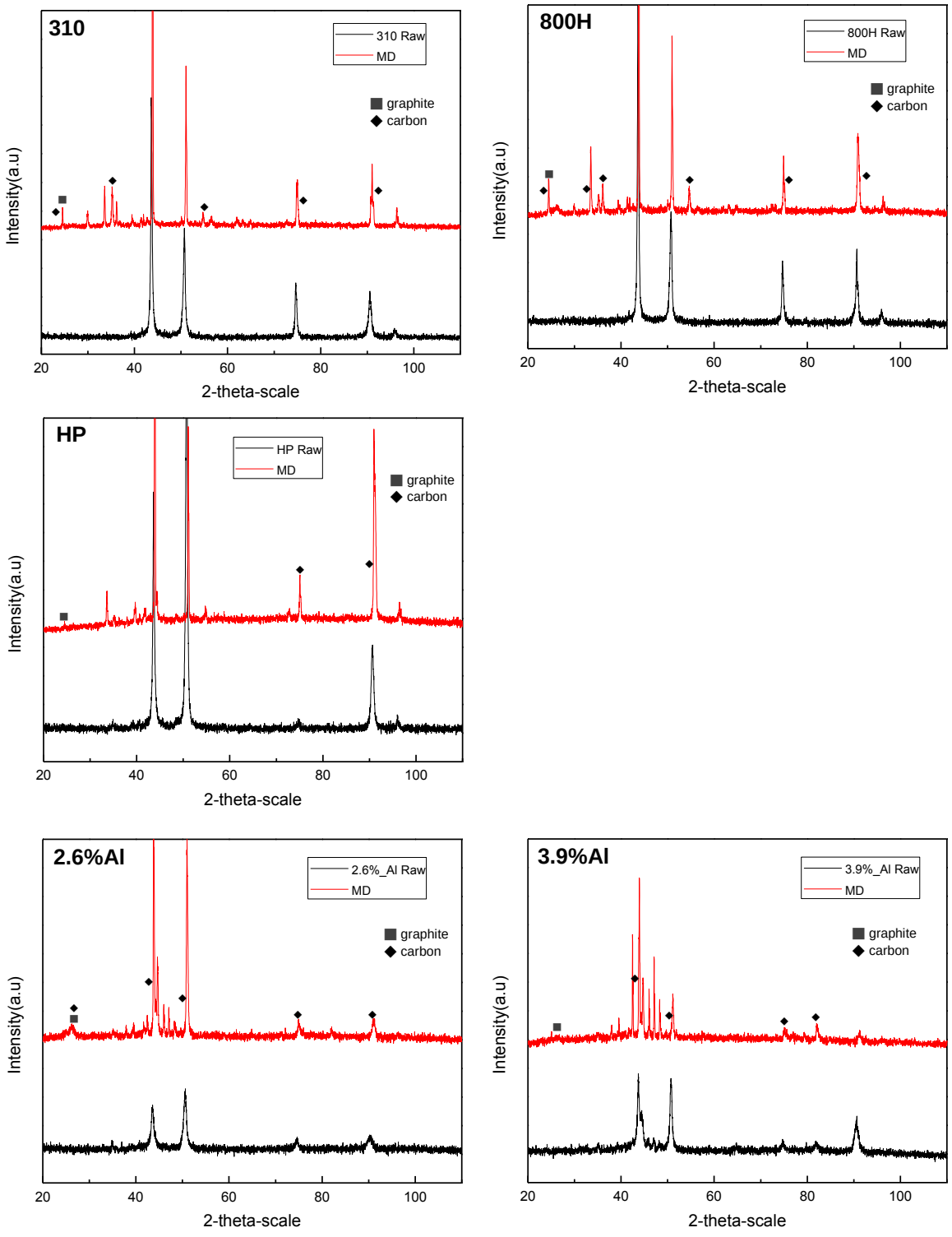

Figure 43. XRD diagrams obtained by analyzing alloys' surface after exposure to metal dusting environment (MD)

CHAPTER 4. ANALYSIS AND DISCUSSION

Five different alloys were exposed to three high-temperature gaseous conditions which are: pure steam oxidation at 950°C for 30 hours (Ox), same oxidation treatment but following with metal dusting treatment at 650°C for 500 hours (Ox+MD), and only metal dusting treatment at 650°C for 500 hours (MD). The formation of oxide layers, carbon attack, and pit formation are the main subjects that we want to observe and study. Samples exposed to the oxidation treatment all formed oxide layers on the surface and internal oxidation beneath the surface. From the general SEM cross-section images results, we can identify that uniform oxide layers were formed and cover on the top, while SEM top-view images would reveal if the surface was really covered with oxide layer and combined with EDS elemental analysis, the surface compositions could be observed. The simplified results of the formation of oxide layer and internal oxidation were sorted into tables and shown in Table 6 and Table 7 for comparison. For alloy 310, there was a relatively thin oxide layer of ~1.5 μm thickness formed upon the surface that consisted of mostly chromium, and also had white pillar-shaped manganese oxide and silicon oxide structures. Beneath the surface of alloy 310 there were some cracks being formed as a result of internal oxidation that consisted of mostly silicon oxide. For alloy 800H, a relatively thicker oxide layer of ~2.7 μm thickness was formed that consisted of chromia and deeper internal oxidation cracks that consisted of aluminum and titanium oxide. From having an initial observation on the cracks through microscope, the internal oxidation cracks for alloy 800H seems to be more severe. For the HP alloy, some areas of the oxide layer fell off (spalled) as indicated by counting the mass change and doing surface observation. Different from alloy 800H, alloy 310, and HP, the AFA alloys formed a more uniform oxide layer on the top through the observation of cross section, top view, and elemental analysis. XRD analysis also show that Cr_2O_3, as

a dominant oxide layer, was formed by the oxidized treatment for not only chromia formers but also alumina formers AFA. The topic that will need to be further discussed will be, for both 2.6%Al and 3.9%Al, alumina formed just underneath the main oxide layer and close to internal oxidation areas. This question was speculated to be caused from either the thickness of the AFA samples which were about only 1.3 mm and it might be too thin compared to the specimens tested by other researchers (27) of the same alloy that were found to form aluminum oxide. The thickness, could limit the amount of aluminum present in the sample to form a uniform oxide layer.

Table 6. Oxide layer formation and average thickness results

Oxidation Test	TEMP (°C)	TIME (h)			
	950	30			
Alloys	310	800H	HP	2.6%Al	3.9%Al
Oxide layer composition	mostly chromia	mostly chromia	chromia	chromia	chromia
Thickness (μm)	1.5	2.7	2.6	2.8	2.7

Table 7. Internal oxidation formation and approximately reached depth results

Oxidation Test	TEMP (°C)	TIME (h)			
	950	30			
Alloys	310	800H	HP	2.6%Al	3.9%Al
Internal oxidation composition	chromia and silicon oxide	alumina and titanium oxide	chromia and silicon oxide	alumina	alumina
Depth (μm)	8.9	14.2	8.8	8.5	5.8

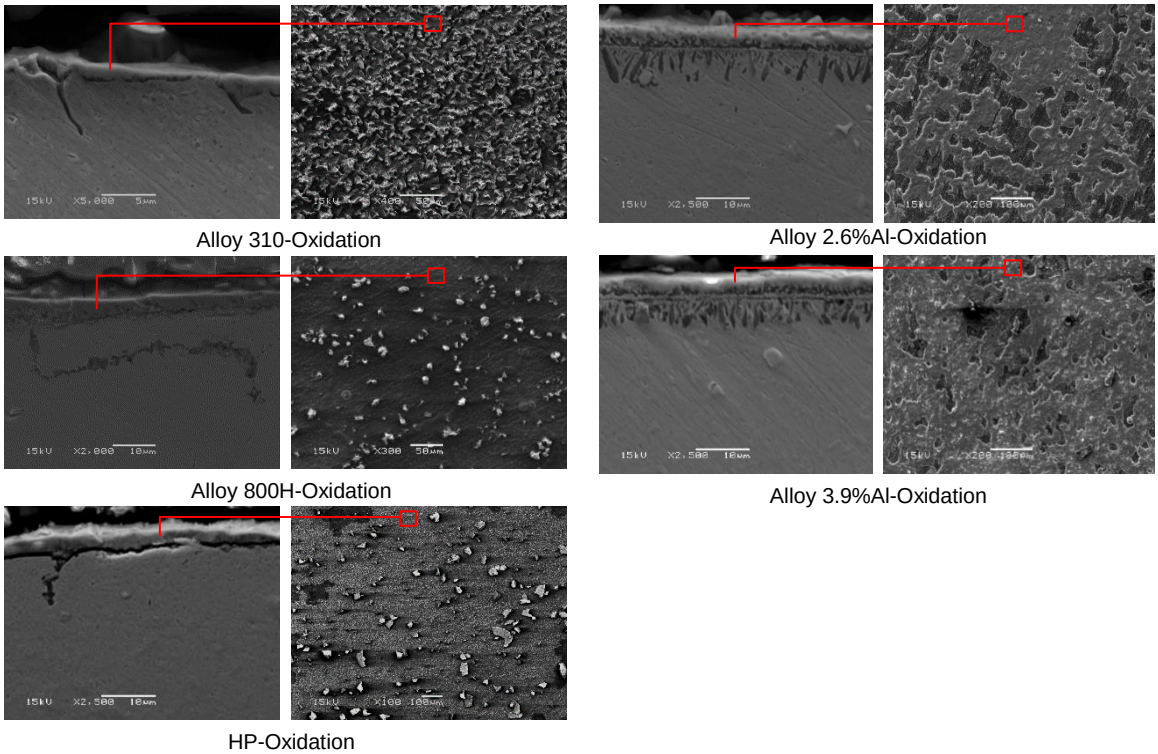

Alloy 310-Oxidation

Alloy 2.6%Al-Oxidation

Alloy 800H-Oxidation

Alloy 3.9%Al-Oxidation

HP-Oxidation

Figure 44. Positions mapping of the SEM images of post-oxidation samples, cross-section image(left); top-view image(right)

In the metal dusting test, there were two items of interest: 1. What is the effect of pre-oxidation on alloy performance in a metal dusting environment and 2. Comparison of the AFA materials to more traditional chromia-forming alloys. In comparing between Ox+MD and MD conditions, it seemed that pre-oxidation treatment will degrade the stability of the structure and increase metal dusting corrosion on the surface. As seen in Figure 44, for alloy 800H, the pre-oxidized samples revealed a severe attack after the metal dusting compared to only metal-dusting treated samples. For AFA alloys, although the oxide layers formed on the top could be protective to metal dusting attack, it seemed that the oxide layers formed by the pre-oxidized treatment will be damaged by the following metal dusting reaction and create a hole-like nodule filled with chromia and alumina. Additionally, the effect of bulk composition on metal dusting performance was observed. By first applying the equation theoretically calculated by researchers (7) based on the content of chromium, silicon, and aluminum, we can predict that alloy 800H will be the most fragile when exposed to metal dusting while the AFA 3.9%Al alloy will be the most stable, as listed in the table 8. After the observing the actual performance (as illustrated in Figure 45), the resistivity to metal dusting reaction of these alloys were quite consistent with the prediction.

Table 8. Theoretical equation applied to predict the resistivity to metal dusting (7)

Theoretical metal dusting resistivity equation	Resistible if, Cr% + 3 × (Si% + Al%) > 24 [7]
Alloy 310	24.52% + 3 × (0.6%) = 26.32
Alloy 800H	20.63% + 3 × (0.3% + 0.54%) = 23.15
Alloy HP	26.52% + 3 × (1.3% + 0.02%) = 30.48
Alloy 2.6%Al	28% + 3 × (1.3% + 2.62%) = 39.76
Alloy 3.9%Al	27.40% + 3 × (1.4% + 3.9%) = 43.3

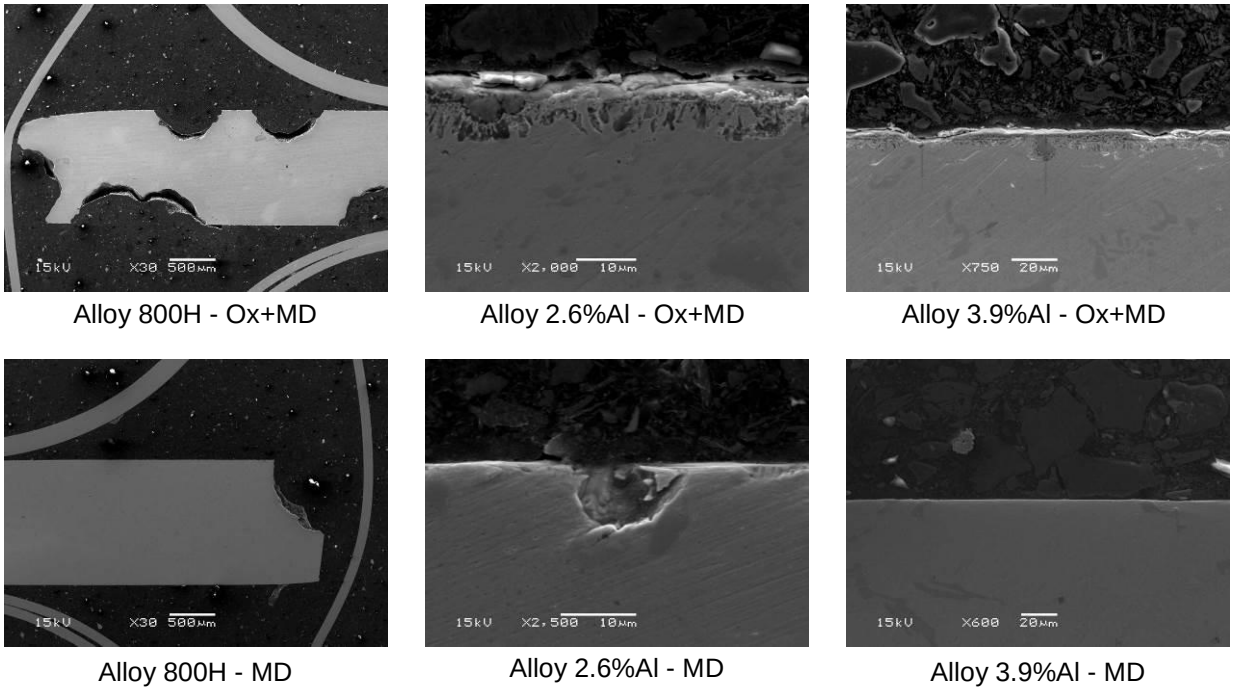

Alloy 800H - Ox+MD | Alloy 2.6%Al - Ox+MD | Alloy 3.9%Al - Ox+MD

Alloy 800H - MD | Alloy 2.6%Al - MD | Alloy 3.9%Al - MD

Figure 45. Comparison of samples went through pre-oxidation plus metal dusting, and went through only metal dusting, Oxidation+ Metal dusting(upper images); Only metal dusting(lower images)

CONCLUSIONS

Heat-resistant cast alloys designed to form aluminum oxide scales were compared to traditional HP and Fe-based alloys for performance in metal dusting conditions.

High temperature oxidation with pure steam atmosphere at 950°C showed the formation of oxide layer and internal oxidation corrosion to the alloys. Formation of a thick oxide layer (~2.7 μm) of chromia was found on all alloys, while alumina-forming alloys further formed a thick, non-uniform internal oxidation layer (~6 μm) of alumina beneath the surface chromium oxide layer. The reason why alumina formers also formed mostly chromia as oxide layer was speculated to be due to the specimen thickness (only ~1.3 mm) which was ten times thinner than the specimens previously used by others (27) and shown to form alumina. However, the oxidation test results also indicate that the different durability of alloys toward high temperature oxidation corrosion.

In only metal dusting exposure to $CO/H_2/CO_2$ atmosphere at 650°C, five different alloys showed different resistance to carbonaceous attacks. For alloy 310, only few damages to the depth of 5 μm showed up as initial stage of pitting attack. Different from alloy 310, 800H showed deep pits of around 500 μm indicating much more severe attacks caused from metal dusting. Alloy HP only showed some small scratches of few micrometers as initial pits caused by metal dusting. The different damaging levels of these chromia formers after exposure to metal dusting could be concluded from one of the reasons that caused by different chromium content in the chemical composition. For AFA alloys, they could still be found initial pits of around 5~10 μm in depth in alloy 2.6%Al, while alloy 3.9%Al almost not being attacked on the surface in this exposure environment which indicated that higher aluminum content could result in better resistance to metal

dusting.

In the oxidation continued with metal dusting test. For alloy 310, pits deeper than 12 μm (2 times larger than only metal dusting) were found. For alloy 800H, not only deeper pits were found, the numbers and regions of attacking pits were large indicating it was attacked severely. For HP alloy, it decomposed to little pieces and mixed together with carbon. Its behavior should be studied more in the future by setting more conditions for HP test, for right now, it can only be said that running metal dusting test to pre-oxidized HP might cause severe attacks and result in break down or even reformation. AFA alloys showed inner corrosions following the direction of internal oxidation areas, and for both 2.6%Al and 3.9%Al, a hole of nodules consisted of chromia and alumina showed up in the interface indicated the corrosion happened to the inner area. Based on these observation, we can conclude that these internal oxidation formations in the pre-oxidation process will increase metal dusting attack and reduce the alloy's performance despite the protective effects expected by the presence of the oxide layer. Based on the observation of these three kinds of exposure environment of the alloys, we can further realize that it is important to try to form a specific protective layer (i.e. alumina layer etc.) by optimizing, meanwhile need to consider about the multiple corrosion attacks given by oxidation and metal dusting exposures.

FUTURE WORK

Study more factors and the optimization of alumina layer formation for the AFA materials should be performed. Factors such as bulk metals thickness or higher temperature (>1050 °C) should be considered. It is speculated that the AFA specimens' thickness might affect the formation of protective alumina layer.

Oxide layers formed on the surface could be identified more clearly using equipment such as X-ray Photoelectron Spectroscopy to further understanding the elemental composition, chemical and electronic states of the elements.

Metal dusting corrosion tests could be improved through design of a more suitable cyclc conditions or longer duration metal dusting exposure times to obtain more severe corrosion results. Varying the gas composition used in the metal dusting test could also be used to get a better results of metal dusting corrosion. More detailed observation could be done through using equipment such as Transmission Electron Microscope to observe the carbon filaments attached on the metals and further understand dusting situations.

REFERENCES

1. Kunio Hirotani. (2005). “Metal Dusting - Severe Problem in Operation of Syngas Generation for GTL Plant”. *The Fifteenth International Offshore and Polar Engineering Conference,* 19-24 June, Seoul, Korea.
2. H. J. Grabke. (1998). “Thermodynamics, mechanisms and kinetics of metal dusting”. *Materials and Corrosion*, Volume 49, Issue 5 May 1998 Pages 303–308.
3. Peter Szakálos. (2004). “Mechanisms of Metal Dusting”. *Doctoral Thesis*, ISBN 91-7283-713-6. Department of Material Science and Engineering, Royal Institute of Technology, Stockholm, Sweden.
4. J. Zhang, D.M.I. Cole, and D.J. Young. (2005). “Alloying with copper to reduce metal dusting of nickel”. *Materials and Corrosion*, Volume 56, Issue 11 Pages 745–834
5. Y. Nishiyama, K. Moriguchi, N. Otsuka, and T. Kudo. (2005). “Improving metal dusting resistance of transition-metals and Ni-Cu alloys”. *Materials and Corrosion*, Volume 56, Issue 11 November 2005 Pages 806–813
6. M.P. Brady, G. Muralidharan, D. N. Leonard, J.A. Haynes, R.G. Weldon, and R.D. England. (2014). “Long-Term Oxidation of Candidate Cast Iron and Stainless Steel Exhaust System Alloys from 650-800°C in Air with Water Vapor”. *Oxidation of Metals*, Volume 82, Issue 5–6 December 2014, pp 359–381
7. SCHILLMOLLER C. M.. (1986). “Solving high-temperature problems in oil refineries and petrochemical plants”. *Chemical engineering*, Volume 93, 1986 Pages 83-87

8. Yoshitaka NISHIYAMA, Koji MORIGUCHI, Hirokazu OKADA, Takahiro OSUKI, Shinnosuke KURIHARA. (2015) “Development of Metal Dusting Resistant Alloy for Synthesis Gas Production Plants”. *NIPPON STEEL & SUMITOMO METAL TECHNICAL REPORT*, No. 107 FEBRUARY 2015
9. Gas Exporting Countries Forum. GECF Global Gas Outlook 2040. (2017). Available from: http://www.gecf.org
10. R.F. Hochman. (1972). “Basic studies of metal dusting deterioration in carbonaceous environments at elevated temperatures”. *Proceedings of the. of the 4th International Congress on Metal Corrosion*, Amsterdam, The Netherlands, pp. 258-263.
11. National Research Council. (1970). “High-Temperature Oxidation-Resistant Coatings: Coatings for Protection From Oxidation of Superalloys, Refractory Metals, and Graphite”. *The National Academies Press*, Washington, DC, p. 223.
12. Samal, Sneha, Zaki Ahmad[book auth.]. (2016). "High Temperature Corrosion" ISBN 978-953-51-2508-2
13. Grabke, H. J., Müller-Lorenz, E. M., & Schneider, A. (2001). “Carburization and Metal Dusting on Iron” *ISIJ International*, Vol. 41 2001 No. Suppl P S1-S8.
14. M.P. Brady, Y. Yamamoto, M.L. Santella, P.J. Maziasz, B.A. Pint, C.T. Liu, Z.P. Lu, and H. Bei. (2008). “the Development of Alumina-Forming Austenitic stainless steels for high-temperature structural Use”*. Journal of Materials Science*, 60(7), 12–18.
15. R.F. Hochman. (1972). “Basic studies of metal dusting deterioration in

carbonaceous environments at elevated temperatures", *Proc. of the 4th Int. Congress on Met. Corr*, Amsterdam, The Netherlands, 1969, pp. 258-263.

16. A Hultgren, M Hillert. (1953). "Betingelser för bildning av cementit vid uppkolning av nickelstål (Conditions for cementitization of nickel steel)". Jernkont. Ann. 1953, 137, 7.
17. E Pippel, J Woltersdorf, HJ Grabke. (1995). "Microprocesses of metal dusting on iron". *Steel Research International*, Volume 66, Issue 5 May 1995 Pages 217–221.
18. P. Szaka´los, R. Pettersson, S. Hertzman. (2002). "An active corrosion mechanism for metal dusting on 304L stainless steel". *Corrosion Science*, Volume 44, Issue 10, October 2002, Pages 2253-2270.
19. E. Pippel, J.Woltersdorf, R. Schneider. (1998). "Micromechanisms of metal dusting on Fe-base and Ni-base alloys", *Mat. and Corr*., Vol. 49, No 5, pp. 309-316
20. Szakálos, P., Lundberg, M., & Pettersson, R. (2006). "Metal dusting on an alumina forming Ni-base alloy". *Corrosion Science*, 48(7), 1679–1695.
21. Aurelie Rouaix-Vande , Kinga A. Unocic, Michael P. Brady, Bruce A. Pint. (2014). "Performance of chromia- and alumina-forming Fe- and Ni-base alloys exposed to metal dusting environments: The effect of water vapor and temperature". *Corrosion Science,* Volume 92, March 2015, Pages 58-68
22. C.M. Chun, J.D. Mumford, T.A. Ramanarayanan. (2002). "Mechanisms of Metal Dusting Corrosion of Iron", J. Electrochem. Soc. 149 7. B348-B355
23. C. H. Toh, P. R. Munroe, and D. J. Young. (2002). "Metal Dusting of Fe–Cr and Fe–Ni–Cr Alloys under Cyclic Conditions". *Oxidation of Metals*, Vol. 58,

Nos. 1/2, August 2002.

24. F.M.L. Mulaudzi, L.A. Cornish, G.A. Slabbert, and M.J. Papo. (2012). “Metal dusting on Alloys 602CA and 800”. *The Journal of The Southern African Institute of Mining and Metallurgy*, VOLUME 7A. Pages 589-600.
25. G. Muralidharan, Y. Yamamoto, M. P. Brady, L. R. WalkerH, M. Meyer III, D. N. Leonard. (2016). “Development of Cast Alumina-Forming Austenitic Stainless Steels”. *Journal of Materials Science*, November 2016, Volume 68, Issue 11, pp 2803–2810
26. Michael P. Brady, Yukinori Yamamoto, Govindarajan Muralidharan, Hiram Rogers and Bruce A. Pint. (2013). “Deployment of Alumina Forming Austenitic (AFA) Stainless Steel”. *Oak Ridge, TN* : Oak Ridge National Laboratory, September 30, 2013.
27. Elmer A. Prenzlow. (2016). “High Temperature Oxidation of Alumina Forming Cast Austenitic Stainless Steels Within an Environment of Pure Steam”. Thesis. University of Wisconsin-Milwaukee.
28. Aurelie Rouaix-Vande,, Kinga A. Unocic, Michael P. Brady, Bruce A. Pint. (2015). “Performance of chromia- and alumina-forming Fe- and Ni-base alloys exposed to metal dusting environments: The effect of water vapor and temperature”. *Corrosion Science*, Volume 92, March 2015, Pages 58-68.
29. Jianqiang Zhang, David J. Young. (2008). “Coking and Dusting of Fe–Ni Alloys in CO–H2–H2O Gas Mixtures”. *Oxidation of Metals*, October 2008, Volume 70, Issue 3–4, pp 189–211

APPENDIX A – FULL COMPOSITION OF FIVE ALLOYS

The full chemical composition data of alloy 310 were provided by Columbia Metals, and alloy 800H were provided by Allegheny Technologies Incorporated, while alloy HP, alloy 2.6%Al, and alloy 3.9%Al were provided by MetalTek.

Table 9. Alloys' full composition

	Alloy				
Element	310	800H	G2553 (HP)	G3607-A (2.6%Al)	G3610-A (3.9%Al)
Al	-	0.54	0.02	2.62	3.9
B	-	-	-	0.001	0.002
C	0.048	0.07	0.44	0.425	0.436
Co	0.020	0.04	0.0715	0.0417	0.0431
Cr	24.52	20.63	26.52	27.9996	27.396
Cu	0.04	0.04	0.08	0.0329	0.0353
Fe	51.0	46.6	35.08	26.8481	24.9261
Mn	1.760	0.64	0.61	0.783	0.795
Mo	0.012	-	0.11	0.171	0.188
N	0.0346	0.011	0.05	0.0403	0.0305
Nb	-	-	0.79	0.7398	0.747
Ni	19.10	30.33	34.5	38.2575	38.0119
O	-	-	0.0583	0.0006	0.0005
P	0.019	0.014	0.017	0.014	0.015
S	0.001	0.0002	0.005	0	0
Si	0.55	0.32	1.26	1.3012	1.4143
Sn	-	-	0.001	0	0.001
Ti	-	0.54	0.09	0.108	0.118
V	-	-	0.051	0.042	0.041
W	-	-	0.1	0.409	1.669
Zr	-	-	0.1	0.115	0.13

Addition : - : not listed

APPENDIX B – DIMENSIONS AND MASS OF SAMPLES

The samples' initial condition before sending to oxidation test and metal dusting test were listed in Figure 10.

Table 10. Samples' dimensions, calculated surface area, and initial mass

	Dimensions (cm)					
Sample	width	length	thickness	height	SA (cm^2)	Mass (mg)
A1	0.594	1.339	0.139	0.10	1.4998	843.35
A2	0.650	1.324	0.136	0.10	1.6298	882.69
B1	0.646	1.383	0.138	0.10	1.7185	932.62
B2	0.635	1.334	0.143	0.10	1.6290	898.58
C1	0.582	1.250	0.136	0.15	1.0108	698.22
C2	0.629	1.399	0.129	0.15	1.3407	828.28
D1	0.652	1.241	0.138	0.10	1.5124	779.82
D2	0.645	1.247	0.147	0.10	1.5366	806.86
E1	0.618	1.220	0.140	0.10	1.3942	728.72
E2	0.570	1.048	0.147	0.10	1.0421	586.68
A3	0.645	1.297	0.140	0.10	1.5885	858.76
A4	0.585	1.382	0.140	0.10	1.5393	844.73
B3	0.618	1.331	0.138	0.10	1.5547	839.44
B4	0.644	1.352	0.131	0.10	1.6360	848.65
C3	0.566	1.354	0.136	0.15	1.1124	710.20
C4	0.627	1.383	0.134	0.15	1.3304	842.73
D3	0.621	1.244	0.137	0.10	1.4277	748.31
D4	0.635	1.245	0.141	0.10	1.4829	787.79
E3	0.615	1.208	0.146	0.10	1.3898	728.85
E4	0.570	1.213	0.148	0.10	1.2822	727.88
A5	0.570	1.360	0.139	0.10	1.4586	817.39
A6	0.678	1.320	0.136	0.10	1.7050	919.37
B5	0.668	1.351	0.142	0.10	1.7500	971.17
B6	0.658	1.457	0.139	0.10	1.8770	971.65
C5	0.636	1.480	0.138	0.15	1.5240	915.25
C6	0.619	1.328	0.134	0.15	1.2233	800.19
D5	0.595	1.250	0.138	0.10	1.3684	735.12
D6	0.709	1.238	0.159	0.10	1.7463	1025.04
E5	0.583	1.119	0.144	0.10	1.1666	645.93
E6	0.726	1.180	0.151	0.10	1.6606	864.29